As of Feb. 2026, this preprint has been accepted for publication in the Geological Society of London special publication “A Tour of the Solid Solar System: Recognizing Early Career Contributions to Extraterrestrial Geology”, linked here.

The appropriate citation is:

A. J. Gawronska, C. L. McLeod, M. Loocke, B. Shaulis. (2026) Evidence for Open Magmatic System Processes Recorded in the Crystal Cargoes of Lunar Basalts. *Geological Society, London, Special Publications 562* (1). https://doi.org/10.1144/gslspecpub2025-14

Full title: Evidence for open magmatic system processes recorded in crystal cargoes of lunar basalts

Abbreviated title: Open magmatic system processes recorded in lunar basalts

A. J. Gawronska[1,*,†], C. L. McLeod[1], M. Loocke[2], B. Shaulis[3]

[1]Department of Geology and Environmental Earth Science, Miami University, Oxford OH, 45056

[2]Chevron Geomaterials Characterization Laboratory, Department of Geology and Geophysics, Louisiana State University, Baton Rouge LA

[3]Trace Element and Radiogenic Isotope Laboratory, University of Arkansas, Fayetteville AR

*Correspondence: ajvgawronska@gmail.com

[†]Current affiliations:

[1]Physics Department, Catholic University of America, Washington DC, 20064

[2]NASA Goddard Space Flight Center, Greenbelt MD, 20771

ORCIDs:

A. J. G https://orcid.org/0000-0002-3470-1177

C. L. M https://orcid.org/0000-0001-8212-2287

M. L. https://orcid.org/0000-0001-7660-2516

B. S. https://orcid.org/0000-0003-0707-8137

Abstract

Basaltic magmatism is fundamental to planetary evolution and establishment of planetary crusts. Decades of terrestrial-based research indicate that basaltic magmatic systems often comprise of a series of discrete magma batches with distinct geochemical compositions. The crystal cargos of magmas erupted from such systems provide evidence of this. Within this framework, we investigate textures and mineral compositions of select Apollo basaltic samples to advance our understanding of extraterrestrial magmatic system evolution. We find that samples 10057, 12043, 15085, and 70017 contain reversely zoned clinopyroxene grains in textural disequilibrium alongside grains that do not record disequilibrium textures or reverse elemental stratigraphies; additionally these samples contain reversely zoned feldspars alongside grains normally zoned in An content and Sr. These populations are reflective of magma mixing processes and introduction of antecrysts, indicating the existence of multiple populations is a result of changing melt conditions. The identified textures are consistent with generation in systems whose architectures comprise multiple distinct magma lenses, where material was transported between distinct environments via porous flow and mobilized by influx of hot, primitive magma. Future work should consider this magmatic framework when investigating the role of crust-forming basaltic magmatism on the Moon and on other planets.

Supplementary material: Supplementary material includes 1) energy dispersive spectroscopy (EDS) maps of the thin sections, 2) a Microsoft Powerpoint that indicates locations of grains where quantitative compositional data was collected, 3) "Annotated Images" that show where spot analyses were completed on individual analyzed grains, 4) an Excel workbook with all compositional data collected via EPMA and LAICPMS. Supplementary material is available at https://doi.org/10.17632/b49p7nc792.1

1 Introduction

The only direct sampling of extraterrestrial magmatic system products with well-documented field context occurred on the Moon during the Apollo and Luna programs between 1969 and 1972 (e.g., Stooke 2017; Yang and Zhao 2018), and more recently by Chang'e 5 and 6 (e.g., Qian et al., 2021; Shen et al., 2025). Whole rock analysis of lunar basalts has been combined with remote sensing evaluation of the physical extents of lunar lava flows to further estimate magma ascent rates and viscosities, with implications for eruption and emplacement mechanisms of extraterrestrial lavas (e.g., Wilson, 2009, Gawronska et al., 2022). Over decades of study, researchers have observed several distinct geochemical differences between suites of lunar basalts. Overall, lunar basalts vary with respect to their whole rock TiO_2 contents (<1 wt. % to 14 wt. %), Al_2O_3 contents (5 wt. % to 20 wt. %), and K_2O contents (below detection limit to 15,000 ppm; Papike et al., 1976; Neal and Taylor, 1992; Shearer et al., 2006). These compositional ranges have been interpreted to reflect partial melting of a compositionally stratified lunar mantle characterized by vertical and lateral heterogeneities. Such heterogeneities are believed to have been established during primordial Lunar Magma Ocean (LMO) solidification, which worked to differentiate the Moon into the feldspathic crust, a K-, REEs-, and P-rich reservoir known as urKREEP beneath the lunar crust, and a stratified mantle composed of olivine and pyroxene cumulates with variable amounts of ilmenite and armalcolite (see McLeod and Gawronska, 2022, for a recent summary). Partial melting of these initially stratified, and later overturned cumulates has been proposed to generate the compositional differences in the sampled basaltic suite. Work performed to understand lunar magmatic systems has generally only included processes of fractional crystallization or crustal assimilation, and has otherwise focused on understanding the LMO theory and resulting lunar mantle cumulates (see

recent reviews by Gaffney et al., 2023, and Shearer et al., 2023), and not magmatic differentiation processes operating to change mare basalt properties during ascent. However, heterogeneities in lunar basalt compositions may not be wholly representative of their source regions, and may instead reflect open magmatic system processes and the assembly of multiple crystal cargoes each with their own unique petrogenetic history, as has been documented on Earth (e.g., Ubide et al. 2014). Textural analysis of lunar basalts via crystal size distributions also indicates that processes like magma mixing may have affected lunar melts prior to eruption, using 2D (Donohue and Neal, 2015; Neal et al., 2015; Xue et al., 2021) and 3D (Gawronska et al., 2022) investigations. It is thus imperative to investigate the crystallization histories of lunar basalts while considering the terrestrial framework, which can work to enhance scientific understanding of the magmatic processes like mixing, mingling, or recharge, that could occur on other differentiated objects. This approach aims to provide new insights regarding the degree to which such processes may have affected the final compositions of lunar basalts sampled at the surface, and thus whether their compositions are representative of their source regions

1.1 Insights from terrestrial systems on basaltic magmatism

Basaltic magmatism is a fundamental process of planetary differentiation, evolution, and crustal (re)surfacing (BVSP, 1981, Wilson, 2009). As direct products of mantle partial melting, basaltic lavas have provided a wealth of information regarding the make-up and evolution of Earth's mantle, the generation of secondary basaltic crusts, and the architecture of magmatic systems and processes operating within them. This has been made possible through decades of detailed mineralogical, textural, geochemical, and geochronological analyses, coupled with observations over a range of temporal and spatial scales thanks to detailed interdisciplinary studies (BVSP, 1981; Jerram and Davidson, 2007; Lee et al., 2009; Marsh et al., 2009;

Middlemost, 2014; Cashman, 2015; Cashman et al., 2017; Ogawa, 2018; Edmonds et al., 2019; Sparks et al., 2019). Recent 10^2 to 10^3 m-scale geophysical investigations of terrestrial magmatic systems indicate that magmas are generally not stored in large-scale chambers (see recent discussions by Edmonds et al., 2019; Sparks et al., 2019; Paulatto et al., 2022). Recent work suggests this is true at hotspot volcanoes such as Hawai'i (Wilding et al., 2023), which is often invoked as one of the best analogs for lunar mare eruption dynamics (e.g., Head, 1976; Spudis et al., 2013). Detailed textural and microgeochemical analysis confirms this, as researchers have recognized that magmas are stored as distinct batches within lenses. Lenses can connect to form trans-crustal magmatic systems (e.g., Cashman et al., 2017; Edmonds et al., 2019; Sparks et al., 2019), or can exist as small, isolated lenses that are mushy over much smaller scales than a trans-crustal framework (i.e., Maclennan 2019). In this framework, magma batches evolve separately and produce crystal cargoes that record unique petrogenetic histories. As they cool, melts produce crystal frameworks – the resulting interstitial melts stored in crystal frameworks are defined as mushes (Cashman et al., 2017; Sparks et al., 2019). Upon remobilization during transport and ascent, batches have the potential to mix and mingle, exchanging molten (liquid) and solidified (crystals) material to produce a new carrier (or host) magma with a distinct cargo (i.e., Fig. 1; Cashman et al., 2017; Edmonds et al., 2019; Sparks et al., 2019, and references therein). Additional contamination of the carrier magma by surrounding wall rock can further influence final whole rock compositions. As a result, the whole rock compositions of lavas erupted at the surface are not always direct indicators of their source regions but more so of the physio-chemical processes that work to change magma composition over time (i.e., mixing, assimilation, fractionation; Blundy and Shimizu, 1991; Davidson et al., 2007; Ginibre et al.,

2007; Higgins and Roberge, 2007; Jerram and Davidson, 2007; Ubide et al., 2014; Ogawa, 2018; Zellmer, 2021).

1.2 Magmatic System Framework

Grain textures along with element partitioning and diffusion behaviors as they relate to temperature, pressure, and melt composition (with or without volatiles) can be used to evaluate the petrogenetic history of a magma's crystal cargo (Blundy and Wood, 1991; Ginibre et al., 2002; 2007; Ustunisik et al., 2014; Jerram et al., 2018; Neave and Maclennan, 2020). One mineral phase that is commonly evaluated is plagioclase feldspar, owing to its ubiquity in magmatic systems, its relative compositional simplicity, and the wealth of feldspar geochemical data across different systems (e.g., Grove et al., 1984; Blundy and Wood, 1991; Ginibre et al., 2007). In plagioclase feldspar for example, a temperature increase can lead to resorption and rounded crystal habits, a decrease can lead to skeletal and acicular morphologies potentially with higher An content, whereas a constant temperature will create near-uniform compositions in plagioclase from core to rim (Lofgren et al., 1974; Ginibre et al., 2007; Mollo et al., 2011). Meanwhile, pressure effects are generally related to decompression during ascent – for example, with decreasing pressure and constant temperature, Na_2O partitions more readily into melt than CaO, generating plagioclase that is more An-rich (Blundy and Wood, 1991; Ustunisik et al., 2014). Otherwise, resorption without significant chemical change in the crystal can indicate rapid change in temperature or decompression/degassing (Ginibre et al., 2007). Plagioclase An content is a good measure of primary compositions because Ab-An inter-diffusion is too slow to be modified during cooling of most magmatism rocks relative to the exchange of other elements (i.e., Na-K; Grove et al., 1984; Costa and Morgan, 2011). Evaluation of complementary trace element abundances can help to evaluate crystal cargo petrogenesis further. For example, the Sr

151 partition coefficient in plagioclase is strictly dependent on plagioclase CaO content and not
152 pressure or temperature parameters. Increasing plagioclase Sr content from core to rim will only
153 reflect changes in the composition of the melt due to processes like mixing, and not mechanisms
154 like ascent (e.g.,, Blundy and Wood, 1991; Berlo et al., 2007; Ginibre et al., 2007; Bezard et al.,
155 2017). Evaluation of rapidly-diffusing elements like Mg from core to rim in plagioclase can
156 additionally inform recent changes in melt composition (on the order of weeks; Moore et al.,
157 2014). While the above approaches to studying the petrogenetic history of one mineral phase
158 have the potential to inform the evolution of the magma during the growth of that one phase,
159 these inferences are arguably strengthened by considering additional phases within the same
160 erupted or emplaced units whose crystallization windows may potentially combine to span the
161 entire petrogenetic history of the magma.

162 In pyroxene, decompression during ascent can also trigger crystal breakdown via
163 dissolution (Neave and Maclennan, 2020). In such a case, resorption without chemical change in
164 the remaining portion of the crystal would be recorded, indicating either temperature disturbance
165 or degassing/decompression (Neave and Maclennan, 2020; Streck, 2008). Interactions with hot,
166 compositionally more primitive magmas (i.e., due to mafic recharge) can also cause dissolution
167 in pyroxene, but could additionally be recorded by a subsequent growth zone with increased
168 MgO and Cr content following the influx of primitive magma (Ubide and Kamber, 2018).
169 Interaction with a magma of distinct composition could therefore influence the compositions of
170 new growth zones away from what would otherwise be predicted by closed-system fractional
171 crystallization models (e.g., Lissenberg et al., 2019). An integrated approach that utilizes textural
172 and chemical information across multiple phases has been repeatedly shown to provide new
173 insights and constraints on the physiochemical processes that contribute to the evolution of a

magmatic system's crystal cargo (e.g., Davidson et al., 2007; Jerram and Davidson, 2007; Zellmer, 2021). This type of work has been accomplished for samples originating from various tectonic settings on Earth including intraplate (Ubide et al., 2014; Coote and Shane, 2018; Couperthwaite et al. 2020), volcanic centers related to subduction zones (Salisbury et al., 2008; Kent et al., 2010; Ginibre et al., 2007; Velázquez Santana et al., 2020, and references therein), and mid-ocean ridges (Moore et al., 2014; Lissenberg and MacLeod, 2016; Bennett et al., 2019).

Crystal morphologies as a result of changing conditions have most recently been summarized in Zellmer (2021) who also outlines specific terminology associated with the petrogenetic history of a crystal. This terminology is utilized throughout this work. Briefly, mineral grains that grew within their host carrier magma are referred to as autocrysts, mineral grains incorporated from distinct but petrogenetically related magmas are referred to as antecrysts, and foreign grains originating from the surrounding wall rock are referred to as xenocrysts (Fig. 1). Antecrysts can generally be identified through observation of reaction textures and, unlike autocrysts, can be reversely zoned from core to rim in major and/or trace elements (e.g., Ubide et al., 2014). A grain with only reaction and/or breakdown texture but no accompanying compositional change recorded during growth from core to rim may instead record breakdown during ascent, not mixing or mingling (e.g., Neave and Maclennan, 2016).

1.3 Sample descriptions

Here, we begin to evaluate the petrogenesis of basaltic lunar magmas through an integrated mineralogical, textural, and geochemical investigation of a diverse suite of Apollo samples that represent a wide range of landing sites and compositions. Through the characterization of textures and chemistries preserved in mineral grains in this suite of Apollo basalts, we first evaluate whether crystal populations with distinct petrogenetic histories are

197 preserved. Through identifying distinct crystal populations, we interpret the processes that may
198 have contributed to sample petrogenesis (i.e., mixing in an open system vs convection in a closed
199 system), discuss the implications for the evolution of magmatic systems on planetary bodies that
200 lack plate tectonics, and recommend future research directions. Samples were chosen for this
201 study based on their textural and whole rock chemical diversity (see Table S1). Samples include
202 10057, 12038, 12043, 15085, 15556, and 70017. To perform the work described we were allotted
203 thin sections 10057,67; 12038,63; 12043,15; 15085,16; 15085,24; 15085,26; 15556,28;
204 15556,241; and 70017,123. Because subsamples originate from the same parent sample, we will
205 describe findings within the context of the samples and not the specific splits unless the split
206 itself impacts findings. Detailed descriptions of sample characteristics (textures, mineralogy),
207 ages, and summaries of previous work can be found in Meyer (2016). Brief descriptions are
208 provided here.

209 Sample 10057 is a vesicular to vuggy, fine-grained (Figs. 2-3) high-Ti basalt, and is
210 categorized as an Apollo 11 group A basalt owing to its enrichment in K and the rare earth
211 elements (REEs, e.g., Jerde et al., 1994). This sample is hypocrystalline with a minor
212 mesostasis/glass component (3.30-8.04% modally). Sample 12038 is an Apollo 12 medium-
213 grained, granular, low-Ti basalt with a very minor glassy mesostasis component (<1% modally).
214 12038 is dominated by subhedral to euhedral plagioclase feldspar laths (Fig. 2), and has been
215 categorized as a feldspathic basalt. Sample 12043 was also collected during Apollo 12, and is
216 classified as a low-Ti pigeonite basalt. It has a porphyritic texture with macrocrystic, zoned
217 pyroxene grains surrounded by a feldspar/pyroxene matrix (Fig. 2). Sample 15085 is coarse-
218 grained (Fig. 2), non-vesicular, holocrystalline, and equigranular basalt belonging to the low-Ti
219 quartz-normative basalt (QNB) group collected during Apollo 15. Sample 15556 is also a low-Ti

basalt and represents the olivine-normative Apollo 15 basalts. It is highly vesiculated (~49% by volume, Gawronska et al., 2022) and hypocrystalline with a minor glass component (1 %). 15556 also contains ~2% modally of macrocrystic olivines set in a fine-grained plagioclase/pyroxene matrix (Fig. 2). Sample 15556 is not uniformly vesiculated, and decreases to ~12% vesicularity on one side (Gawronska et al., 2022). The two sections we received are ,241 and ,28; 15556,28 originates from a portion of the sample that chipped off (split ,1) seemingly from the highly vesiculated portion of 15556, while section ,241 originates from split ,112 within the interior of the sample which is also highly vesiculated (Meyer, 2016; R. Zeigler, pers. comm.). Sample 70017 is a medium to coarse-grained high-Ti basalt belonging to the Apollo 17 group B, and contains "chains" of ilmenite (Fig. 2; Paces et al., 1991; Meyer, 2016).

2 Methods

2.1 Microscopy

We used light and electron microscopy to document sample mineralogy and textural characteristics. Thin sections were first characterized using a Leica DM2700 P polarizing light microscope (PLM). Additional data was collected via a Zeiss Supra 35 VP FEG Scanning Electron Microscope (SEM) in-house at the Miami University Center for Advanced Microscopy and Imaging (CAMI). Characterization via SEM involved acquisition of 1) backscatter electron (BSE) images and 2) energy dispersive X-ray spectroscopy (EDS) elemental maps. Both datasets for each sample were collected at a resolution of 2048 by 1536 pixels, a dwell time of 256 µs, a working distance of 10 mm, and an accelerating voltage of 20 keV. Individual images and maps were stitched together using *Illustrator* (Adobe Inc. ©, version 23.0.1). Finally, *ImageJ* (version 1.52a; Schneider et al., 2012) was used to merge individual elemental maps which supported an

initial, qualitative, evaluation of the relationships between mineral textures and chemistries (see Figs. 3, S1).

2.2 Crystal Size Distribution Analysis

Imaging via PLM and SEM facilitated identification of phase boundaries. This spatial context permitted crystal size distribution (CSD) analyses to be performed, enabling evaluation of the crystallization history of each sample. This process has been used to estimate grain cooling histories in terrestrial and extraterrestrial samples (e.g., Higgins, 2000; Morgan and Jerram, 2006; Donohue and Neal, 2015; Neal et al., 2015). The free software GNU Image Manipulation Program (GIMP, version 2.8.18, www.gimp.org) was used to outline each sample, followed by the outlining of individual crystals. During this process, touching crystals remained on separate layers. The outlines were filled, and layers with data were exported from GIMP as images for further analysis. In *ImageJ,* the area of the sample was extracted, along with the measured areas, lengths, and widths of each grain. This data was next processed through the CSD Slice 2.0 Excel spreadsheet (Morgan and Jerram, 2006), then plotted via the *CSD Corrections* program developed by Higgins (2000). *CSD Corrections* first calculated the most likely three-dimensional shape of each grain, and then determined the natural log of population densities as a function of grain long axes. Phases investigated via CSD analysis included plagioclase feldspar and ilmenite. To ensure CSDs of a phase with tabular habit (i.e., plagioclase feldspar) are statistically significant, 200+ crystals must be outlined (Morgan and Jerram, 2006). For this reason, sample 15085 could not be investigated via CSD. Crystal frequencies are summarized in Table S2, and individual CSDs are reported in Fig. S2. As no sample contained a statistically significant number of olivine grains, olivine was not considered.

2.4 Geochemical Analysis

Next, the major element oxide (i.e., SiO_2, CaO, MgO) concentrations of the silicate phases of feldspar, pyroxene, and olivine (where available) were quantified in-situ via electron probe microanalysis (EPMA). This was accomplished on a JEOL JXA-8230 electron microprobe at Louisiana State University. In-situ analyses of trace elements in these phases followed, and were carried out via laser ablation inductively coupled plasma mass spectrometry (LA-ICP-MS) on a NWR193 laser ablation system connected to a Thermo Icap Q ICP-MS at the University of Arkansas. Data was collected as individual spot analyses to ensure that data was "spot-resolved," i.e., the exact location and chemistry of each spot was known and there was no overlap in spots.

3 Results and Discussion

3.1 Apollo 11 high-Ti basalt 10057

Generally, pyroxene and ilmenite in 10057 are equigranular (~0.2 mm), while the feldspar grains range in size and habit from small (~0.02 to 0.2 mm) anhedral, interstitial grains to larger (~0.3 mm) subhedral/euhedral, tabular grains (Figs. 2-3; see also Fig. S3). Both feldspar and ilmenite CSDs have a linear slope, indicating that neither of these phases records a significant change that would otherwise impact crystallization rate during cooling (Fig. 4). Due to the fine-grained nature of this sample, only three plagioclase feldspar grains could be analyzed via LA-ICP-MS at both the core and rim. Considering major element chemistry, we identified one plagioclase grain that is subhedral and tabular (which is texturally representative of other feldspar grains) with reverse zoning in An (core: An_{78}, rim: An_{87}), normal zoning in FeO (core: 0.56, rim: 0.60 wt. %), and an elevated core La/Sm ratio of 4.96, relative to other normally-zoned feldspar crystals (cores: approximately An_{82}, ~0.80 wt. % FeO, La/Sm <3.5; rims: <An_{80}, >0.60 wt.% FeO, La/Sm ~2.5 to 3; Fig. S4). The one reversely-zoned grain also has a ~40 ppm

increase in Sr content from core to rim (Fig. S5). Because reverse zoning in major element content corresponds with changing Sr compositions, this grain is interpreted to record a change in its crystallization conditions during growth, likely due to interaction with a more primitive magma. An additional normally An-zoned crystal also records an increase in Sr at the rim. Both are depleted in other trace elements (i.e., Rb, Sr) relative to a more enriched normally-zoned grain containing elevated REE core contents (Fig. S6) and high La/Y (Fig. S7). Eu/Eu* anomalies were calculated using chondrite-normalized values (after Sun and McDonough, 1989) as Eu/Eu* = $(2*Eu_N)/(Sm_N+Gd_N)$. The Eu/Eu* systematics for this sample record a decrease in Eu/Eu* from core to rim in both of the grains which record an increase in Sr (Fig. S7). The distinct relationship in An vs. La/Y and An vs. Eu/Eu* between the reversely-zoned grain and the normally-zoned grains may indicate that these grains crystallized in distinct magmatic environments. However, these grains are not texturally distinct suggesting they experienced similar cooling histories (consistent with the constant CSD), which may indicate that compositional changes are related to incorporation of material with distinct composition via a process such as mingling, which would not fully homogenize melt composition prior to crystallization. Previous work has proposed that sample 10057 experienced assimilation of KREEPy material during its petrogenesis (Jerde et al., 1994). This is supported by the abundance of K-rich mesostasis, and by approximately half of the feldspar cores analyzed here having elevated trace element contents (i.e., >16 ppm Rb, relative to <5 ppm for the remaining grains, Fig. 5; note that these grains are too small for rim analysis via LA-ICP-MS). Interestingly, one feldspar grain analyzed records a negative Eu/Eu* anomaly. Previous work by Dygert et al. (2020) suggests that negative Eu/Eu* anomalies in plagioclase may be explained by subsolidus re-equilibration following heating by an impact, though neither this grain nor others preserve

other features indicative of impact (i.e., maskelynization). As a whole, 10057 also does not preserve textural evidence of an impact melt origin (Fig. 4). More work is required on this suite to assess this further.

In the pyroxene population, one glomerocryst (Fig. 5; Fig. S3) contains larger grains in comparison to all other pyroxene within this sample: ~0.35 mm vs. <0.2 mm long. As mentioned above there are regions of K-rich mesostasis in this sample, and pyroxenes nearby to this mesostasis preserve reaction textures (i.e., resorption). In BSE, pyroxene grains in the glomerocryst display patchy zoning and limited resorption at the rim which is distinct from the progressive zoning observed in other pyroxenes. In addition, glomerocrystic pyroxenes contain small ilmenite and feldspar inclusions (Fig. 5). One grain in the glomerocryst has close to constant Mg# (core: 74.1, rim: 72.2), while matrix grains range from Mg# 74.1 to 70.4 in the core and Mg# 56.5 to 17.1 in the rim (i.e., showing normal zoning; Fig. 7). Along with one other matrix grain, the grain analyzed within the glomerocryst has relatively higher CaO values in the core (~17 wt. %) relative to other, non-glomerocrystic cores (<15.5 wt. %; Fig. 7). The glomerocrystic grain is additionally depleted in the trace elements Cr, V, and Sc and elevated in REEs in its core relative to other, non-glomerocrystic grains' cores (Figs. 5, S9-S11). Specifically, the grain within the glomerocryst is reversely zoned in Cr, which combined with its texture is interpreted here as recording a magmatic environment that became more primitive, possibly due to influx of primitive magma via recharge (e.g., Costa and Morgan 2011, Ubide and Kamber, 2018, Ubide et al., 2019). Thus, based on its distinct texture and geochemistry, the pyroxene glomerocryst is interpreted here as being antecrystic. Glomerocrysts are theorized to originate from either cumulates or mushes (e.g., Cashman et al., 2017). It is possible that this glomerocryst represents a cumulate layer or mush within a magma lens, and was plucked by

ascending hotter, more primitive melt. In such a scenario a change in composition and temperature would work to unlock the mush (see discussion by Neave et al., 2021 and references therein).

The influx of a primitive melt would result in a change in melt composition that would also be expected to generate reverse An and Sr zoning like that observed in some 10057 plagioclase grains. After rising, this magma with an entrained glomerocryst and reversely-zoned feldspar is inferred to have interacted with a more KREEPy magma batch, generating pyroxene resorption and potentially generating reverse Sc-zoning of one analyzed pyroxene grain that is next to mesostasis (black in Fig. S8). This additionally may have led to incorporation of a distinct feldspar population highly enriched in REEs, and generated the K-rich mesostasis seen in this sample. Nonetheless, we identified only one glomerocryst and more work must be performed on this sample suite (the high-Ti, high-REE basalts of Apollo 11) to utilize novel datasets like 3D XCT to explore potential pyroxene glomerocryst population in this sample suite.

3.2 Apollo 12 feldspathic basalt 12038

In 12038, both plagioclase and pyroxene are seriate, ranging in size from 0.1 to 10 mm (Fig. 2). Feldspar grains range in habit from euhedral tabular grains to subhedral laths, and some are subophitically contained within pyroxene grains (Fig. S3). CSDs performed here record slight upward curves in both plagioclase and ilmenite (Fig. 4), indicating accumulation and/or coarsening. All feldspar grains analyzed have relatively high CaO wt. % cores (An_{82} to An_{86}), high MgO cores (0.26-0.36 wt. %), and low FeO cores (~0.5 wt. %; Fig. S4). In terms of trace elements, plagioclase cores are low in Eu (~2 ppm), and Sr (292.2 to 306.9 ppm) relative to their respective rims, but the difference from core to rim in Eu is <1 ppm, and in Sr <100 ppm except for one subophitic grain (Figs. S5-S7). Eu/Eu* anomaly values for all grains are almost identical

between cores, and between rims (Fig. S7). We interpret this as all analyzed feldspar grains recording the same petrogenetic history (as indicated by similar major and trace element signatures from core to rim), indicating that geochemical signatures that would otherwise be indicative of open system processes are not evident within the studied plagioclase population. Crystallization of feldspar is thus inferred to have occurred under closed system conditions, with grains experiencing either accumulation or coarsening during crystallization (as is supported by CSD work, Fig. 4c).

All pyroxene grains in 12038 are subhedral to anhedral. Some are sieved near the rim and breaking down to 3-phase symplectite (e.g., Fig. S3). All pyroxenes are normally zoned from core to a mantling zone (Fig. S8; average core: $En_{47.2}Fs_{33.1}Wo_{19.7}$, Mg# 58.2; average mantle: $En_{18.6}Fs_{47.1}Wo_{34.3}$, Mg# 28.5), but three out of seven analyzed grains are reversely zoned from mantle to rim with higher MgO and lower CaO towards the rim ($En_{28.2}Fs_{39.7}Wo_{32.1}$, and Mg# 41.6, as opposed to normally-zoned rims of $En_{7.0}Fs_{70.5}Wo_{22.5}$ and Mg# 8.8 of other crystals). This implies they are not in equilibrium with the mesostasis. One grain is additionally reversely zoned in Al_2O_3 from mantle (2.8 wt. %) to rim (3.8 wt. %) relative to other grains (rims: $\leq$2 wt. % Al_2O_3; Fig. S8) suggesting it crystallized before plagioclase (e.g., Grove and Bence, 1977). All grains are normally-zoned in Cr and V, but those with reverse MgO and CaO near their rim also initially increase in Sc by ~20 ppm from core to mantle, and then decrease again in Sc by 60-80 ppm toward the rim to match the Sc core content of a grain with the highest Mg# (66.3) found (Fig. S9). An influx of primitive magma should increase the Cr content at the rim, while mixing with another batch should distinctly affect major and trace element contents, but the element variations here are comparable within and between cores and rims (i.e., Figs. S10-S11). Thus, we conclude that the intragrain geochemical signatures are related to local

379 differences in the melt that may have been produced by movement through a compositional
380 gradient via a process like convection. Pyroxene breakdown can occur from changes in pressure
381 alone during ascent (Neave and Maclennan, 2020), which we invoke here to explain
382 disequilibrium textures (sieving and symplectites; Fig. S3).

383 ***3.3 Apollo 12 pigeonite basalt 12043***

384 This porphyritic sample contains pyroxene macrocrysts (1 to 5 mm) in a matrix of
385 feldspar and pyroxene grains that, in certain locations, are radially growing out of points of
386 common nucleation (Fig. S3). Plagioclase grains are seriate (~0.02 to 0.55 mm) and subhedral to
387 euhedral. Some preserve quenched, skeletal textures, and all are oriented along a flow plane and
388 pushed up against pyroxene macrocrysts (Figs. 2-3). There is a kink in the feldspar CSD
389 suggesting a rapid change in cooling parameters, but not in the ilmenite CSD (Fig. 4). This may
390 indicate that any sudden change in the cooling history of this sample like mixing may have
391 occurred either prior to ilmenite crystallization, or that the ilmenite crystal population is not large
392 (or abundant) enough to have recorded it. Compositionally, feldspar does not record significant
393 changes in An content, but several feldspar grains are normally zoned from high An cores (An_{93-91})
394 to lower An rims (An_{91-90}), while others trend reversely from variably low An cores (An_{91-88})
395 to variably higher An rims (An_{92-89}; Fig. S4). There is only limited correlation between Sr values
396 and An content, suggesting that reverse An is a consequence of rapid decompression during
397 ascent through the system rather than changing magma composition. However, Eu/Eu* anomaly
398 values show the opposite relationship between reversely-An zoned and normally-An zoned
399 grains (Fig. S7), perhaps indicating that grains grew in distinct magmatic environments prior to
400 ascent.

Texturally, at least two populations of pyroxene are defined - the coarse-grained (>0.5 mm long), subhedral to euhedral megacrysts, and the smaller (<0.5 mm long) subhedral to anhedral matrix pyroxenes (Figs. 1-3). Most of the macrocrystic pyroxenes have sieved mantles that correspond to an increase in CaO, and are visibly zoned under polarized light (Figs. 2-3). All pyroxenes here are normally zoned; most macrocrysts have pigeonitic core compositions of Mg# 65.3 and $En_{60-58}Fs_{31-33}Wo_{9-11}$, but two analyzed macrocrysts have elevated CaO in their cores (~16 wt. %) making them augitic in the core ($En_{36-41}Fs_{24-27}Wo_{35-37}$; Mg# 60.2; Fig. 6). Of the pigeonitic group, two grains have mantles that are elevated in CaO (~15 wt. %). Of the augitic grains, one is also enriched in Sc, Cr, and V (109.7 ppm, 8399.8 ppm, 631.9 ppm, respectively) relative to the cores of other pyroxenes crystals (<85 ppm Sc, <6793 ppm Cr, <476 ppm V). Meanwhile, one of the pigeonitic grains with a high-CaO mantle is also elevated in La/Sm in its core (1.5) relative to its rim (0.6) and to other grains (Fig. S9), and in Ce/Y (0.33 core, 0.18 rim) in its core relative to other grains (Fig. S11). This LREE-enriched grain is the largest (5 mm), tabular pyroxene macrocryst visible in Fig. 2; the high CaO grains represent two macrocrysts, while other macrocrysts are similar to matrix pyroxenes. Matrix pyroxenes have core compositions of approximately Mg# 52.4, and $En_{43}Fs_{39}Wo_{19}$.

Between the pigeonitic, augitic, and matrix pyroxenes, three distinct cooling histories of pyroxene may be recorded (Fig. 6). A rising, more primitive magma encountering a separate, possibly mushy lens of more evolved composition could have entrained grains with higher CaO cores, and produced Ca-rich mantles around Mg-rich cores. In this scenario, incorporated Ca-rich melt changed the stability of augite relative to pigeonite (see also Ross et al., 1970; Grove and Bence, 1977; Grove and Juster, 1989). The Ca-rich cores and mantles are interpreted here as antecrystic, having formed in a separate magmatic environment. Remaining macrocrysts are

compositionally similar to matrix pyroxenes in terms of major and trace element contents, but likely formed earlier considering their larger size. Rim compositions of both pigeonitic- and augitic-core grains are similar to each other, and similar to matrix pyroxene core compositions, indicating that matrix pyroxene grew following the mixing of these two liquids. In this framework, introduction of primitive melt may have prompted eruption, which is common on Earth following episodes of mafic recharge in magmatic systems (e.g., Huber et al., 2011, Lissenberg and MacLeod, 2016; Ubide and Kamber., 2018; Sparks et al., 2019; Gleeson et al., 2023). Neal et al., (1994) used assimilation and fractional crystallization modeling to show that 12043, and the remaining Apollo 12 pigeonite basalts, likely assimilated crustal materials of varying compositions during their petrogenesis. This work proposed that the assimilants were likely anorthositic in composition, and may therefore have provided additional CaO for pyroxene formation, and generated plagioclase populations with distinct compositional profiles. Meanwhile, transport from depth, between lenses, and/or leading to eruption may have contributed to the observed disequilibrium textures.

3.4 Apollo 15 quartz-normative basalt 15085

The grains in this sample are too coarse (average grain size of 1 to 5 mm) to attempt a CSD on any mineral phase. Feldspar grains are generally subhedral and interstitial (Figs. 2-3). Approximately one in ten plagioclase grains in this sample are concentrically zoned under polarized light (Fig. 2). Compositionally, cores of feldspar grains have variable An ranging between An_{95} and An_{80}. When comparing composition and texture, three populations become apparent: a normally zoned, reversely zoned, and interstitial plagioclase population (described further below). Of the 18 analyzed grains, eight decrease by 2-3 An mol% from core to rim and are thus normally zoned, but range widely in rim composition from ~An_{90} to An_{78}. Six record

447 reverse zoning where An increases by 1 to 2 mol from core to rim, while four analyzed grains
448 record no change in An from core to rim (Fig. S4). The normally-zoned grains range in habit
449 from euhedral to anhedral and contain numerous small (<0.5 mm) pyroxene inclusions. The
450 reversely zoned crystals are euhedral to subhedral, relatively large (~3.5 to 4 mm), and typically
451 contain fewer pyroxene inclusions. The MgO contents of cores of normally-zoned An grains are
452 relatively depleted (<0.17 wt. %) when compared to the reversely-zoned population (>0.23 wt. %
453 MgO). In addition, the normally-zoned population records an increase in Sr at the rim (by 50 to
454 150 ppm) which would be consistent with the introduction of compositionally more primitive
455 magma. This is not observed in the reversely-zoned grains or the no-change grains, neither of
456 which record any change in Sr from core to rim indicating their An change probably comes from
457 Na-Si dissolution during decompression (Ustunisik et al., 2014). As cooling progressed, a final
458 late-stage interstitial population rich in Eu, Rb, Sr, and low in An formed: this additional
459 population of feldspar grains is euhedral to subhedral, low in An (< An_{85}), high in $NaO+K_2O$
460 (>1.5 wt. %), Eu (>3 ppm), Rb (>0.15 ppm), and Sr (>492 ppm) in their cores relative to the
461 remaining grains (≤ 1 wt. % $NaO+K_2O$, <2 ppm Eu, <0.1 ppm Rb, <300 ppm Sr; see Fig. S5).
462 Thus, this interstitial population is interpreted to represent a late stage of plagioclase growth.
463 These three feldspar populations have similar trace element, and particularly REE, contents
464 (Figs. S6-S7) suggesting that they are likely derived from the same source region. Eu/Eu*
465 systematics show a complex history of feldspar crystallization, with grains of similar An content
466 having opposite Eu/Eu* values, i.e., some with elevated Eu anomaly values (>60) in their cores
467 relative to their rims, and with others having lower Eu anomaly values in their cores relative to
468 their rims (<40; Fig. S7); the late stage population is distinct on the basis of An values, but not
469 Eu/Eu* values.

Texturally, there are at least three pyroxene populations in sample 15085 (Fig. 7). The first displays prominent sieve textures, which are also associated with discrete compositional zones (Figs. 2-3). At the rims of these grains, Fs-Fa-SiO_2 symplectites are also present (and, in extreme cases the pyroxenes have been completely replaced by symplectite, Figs. 7, S3). The second population is characterized by resorbed cores, sieved textures between compositional zones, and displays only minor breakdown to Fs-Fa-Si symplectites. The third population is typically interstitial in nature and comparatively exhibits minimal sieve textures, and no breakdown to symplectite. Generally, pyroxenes in greater textural disequilibrium in 15085 have resorbed MgO- and Cr-rich cores overgrown by Ca-rich mantles, with Fe-rich rims – the transitions between each zone are sieved, and Fe-rich rims are commonly dominated by symplectite. As shown in Figs. 7 and S9, the grain mantles coincide with a 9 to 16 wt. % increase in CaO, a 3 wt. % decrease in FeO (see also Figs. 3, S8), and a ~1000 ppm increase in Cr, 45 ppm increase in Sc, and 300 ppm increase in V (Fig. 8). As seen in Fig. 7B, one such grain is resorbed, and has been completely replaced by symplectites at the rim; compositionally it's low-Ca core (~ 3 wt. % CaO) has an inner mantling zone elevated in CaO (~14 wt. %), and later zone elevated in Cr (5432.7 ppm). This grain is not otherwise distinct in trace elements (Fig. S9), but may also preserve evidence of sector zoning which has been partly destroyed by breakdown.

La/Sm vs. Dy/Yb systematics (Fig. S9) also show potentially three distinct compositions of cores which are not as clearly reflected in other compositional frameworks. The euhedral to subhedral grains in greatest textural disequilibrium (sieved, with occasional symplectite rims; Figs. 7A-B) and the highest core Mg# (>65) and Cr (>4500 ppm) with CaO-rich mantles have generally low La/Sm and Dy/Yb relative to other grains (<0.5, <1, respectively). We conclude that this texturally and compositionally distinct pyroxene population represents a relatively early-

493 formed, primitive, antecrystic population within sample 15085, based on definitions by Edmonds
494 et al. (2019) and Zellmer (2021). The second population of resorbing, anhedral grains, some of
495 which have relatively low Al_2O_3 (~1 wt. %) and high Sc (~50 ppm) compared to other
496 populations' cores (>~3 wt. % Al_2O_3 and <40 ppm Sc), have high Dy/Yb (>1) – this may
497 represent crystallization from a chemically distinct, more evolved melt composition (Fig. 7C).
498 The third group of grains with less extensive sieving have lower Mg# cores (~50), lower Cr
499 (~4000 pm), and higher La/Sm (>0.5) and Ce/Y (Figs. S8-S9, S11) values (Fig. 7D). These are
500 interpreted to represent a later stage of formation based on elevated trace and incompatible REE
501 contents in their cores, or may be entirely distinct considering their high Ce/Y values (see Figs.
502 S8-S11). Moreover, this may be the only population of pyroxenes in 15085 that is in equilibrium
503 with the final carrier magma given the lack of significant sieving or symplectite development.

504 For 15085 pyroxenes, primitive, early-formed MgO- and Cr-rich cores are interpreted to
505 have been transported to a mushy lens where a compositionally more evolved interstitial melt
506 was present. In this environment, they experienced resorption and subsequently grew CaO-rich
507 mantles, while CaO-rich material was incorporated. As crystallization continued in this
508 magmatic environment, the interstitial melt would have become relatively enriched in
509 incompatible trace elements (differentiated) as a result of continued crystallization, perhaps
510 generating the final population with elevated La/Sm and Ce/Y core signatures. These textural
511 and chemical observations are consistent with the conclusions of Vetter et al. (1988) who
512 determined that the Apollo 15 quartz-normative suite which this sample belongs to formed by
513 extensive fractional crystallization of pigeonite, which are now found as phenocrysts throughout
514 the QNB suite; these phenocrystic, early-fractionated pigeonites may be represented here as the
515 early-forming, antecrystic population. Lindstrom and Haskin (1978) additionally argued that

516 mixing of separate magma batches is required to produce the QNB samples, which would
517 account for pyroxene grains with elevated La/Sm and Ce/Y ratios, and plagioclase feldspar
518 grains with distinct Eu/Eu* vs. An relationships. This is also consistent with Snape et al. (2019)
519 who suggested that the quartz-normative Apollo 15 samples could have formed through mixing
520 of distinct magma batches (one primitive, one derived from KREEP). A few pyroxenes in the
521 second (in moderate textural disequilibrium) and third (in minimal textural disequilibrium)
522 populations described here also record an increase in Cr (by 100 to 500 ppm) at the rim, which
523 may correspond to influx of hot primitive magma that would mix with trace element-enriched
524 interstitial melt and unlock and mobilize this cargo. These processes are discussed further in
525 **Section 4**.

526 ***3.5 Apollo 15 olivine-normative basalt 15556***

527 Based on CSD analysis, plagioclase in section 15556,28 records an upward curve
528 consistent with accumulation or coarsening, but plagioclase in section -241 is constant and does
529 not preserve this. Meanwhile ilmenite CSDs indicate a kink in section -28 consistent with
530 multiple crystallization episodes, but no such signature is recorded in 15556,241 (Figs. 4, S2).
531 Section -241 is larger and contains more crystals, thus it is likely more representative.
532 Plagioclase grains are generally equigranular (~0.25 mm), range from subhedral to anhedral,
533 interstitial, and occasionally poikilitically enclose some of the smallest pyroxene grains in this
534 sample (Figs. 3, S3). It is noted here however that some larger feldspar grains (up to 1 mm) do
535 exist in texturally distinct crystal clots throughout this sample (Fig. S3). Some feldspar grains
536 display normal zonation patterns with relatively high An (>An_{91}) and low Na_2O+K_2O (most <0.8
537 wt. %) cores that decrease by ~2 An and increase by up to 0.5 wt. % Na_2O+K_2O towards the rim,
538 while other feldspar grains record slight reverse zoning from lower-An (generally <An_{90}), higher

539 Na_2O+K_2O (~1.2 wt. %) cores that record a 0.5 An increase and decrease of ~0.3 wt. %
540 Na_2O+K_2O toward the rim. The reverse grains are anhedral, and the normally zoned grains
541 subhedral. All grains increase in FeO from core to rim by 0.1 to 1.5 wt. %. Three out of seven
542 normally An-zoned grains, and two of the four reversely An-zoned grains studied here, increase
543 in Sr (by >60 ppm) and Eu (by 0.5 to 2 ppm) from core to rim. Three out of four reversely An-
544 zoned grains also correspond to an increase in Sr from core to rim, which could indicate an
545 influx of new, compositionally primitive magma. However, changes in the major and trace
546 element contents across all studied grains are small; all grains display similar MgO and FeO
547 systematics, and REE contents are consistent between grains (Figs. S6-S7). Therefore, if any
548 influx of new material into the crystallization environment did occur, it likely had a similar
549 composition. Eu/Eu* anomaly values for plagioclase preserve a range of compositional changes
550 from core to rim, with no definitive, overarching relationship between An and Eu/Eu* recorded
551 by the grains in this sample. The various differences in composition across grains studied here do
552 not correspond to textural differences, and the rim compositions of feldspar grains do not
553 converge on a singular composition, but all grains occur within cm of each other (within each
554 thin section of this one sample). This suggests that grains either were incorporated right before
555 eruption, or melt composition differed on a small scale. Local differences in the bulk rock
556 composition of 15556 have previously been attributed to short range unmixing (described further
557 below; Lindstrom and Haskin, 1978).

558 Pyroxenes are generally euhedral to subhedral, and seriate (0.2 to 0.5 mm long). With the
559 exception of one grain, all analyzed grains (n=13) are normally zoned from cores with Mg# of 62
560 to 63 and rims of approximately either Mg# 30 or Mg# 13. There is one grain found here that is
561 interstitial to feldspar, and differs from others with a lower core Mg# (32.9) and higher rim Mg#

(34.7, Fig. S8). The core of this grain also has relatively elevated Sc (94.8 ppm), and lower V (122.1 ppm) and Cr (1232.4 ppm) compared to other grain's cores (<81 ppm Sc, >319 ppm V, >3140.4 ppm Cr, Fig. S9). From Sc contents, two groups of pyroxene grains are defined, where several grains are normally zoned from >75 ppm in the cores, to <66 ppm in the rims. The remaining grains (including the low core Mg# grain) have <53 ppm Sc cores and to up to 90 ppm Sc rims (Fig. S9). Grains with relatively low Sc are generally also low in REE contents (Fig. S10), while those with high core Sc have elevated REE contents, with one grain exhibiting a particularly high Ce/Y (Fig. S11). The low-Sc cores also generally correspond to low Dy/Yb core values of ~1.2, while the high Sc cores generally have higher Dy/Yb values of ~2, with some displaying high La/Sm ratios (>0.4, Fig. S9). Grains that are in textural equilibrium, and grains that are in textural disequilibrium (i.e., lightly sieved and resorbing) exist in both compositional populations (as defined by Sc; see Figs. 2-3, S2). Thus in 15556 pyroxene textures do not readily correlate with unique geochemical signatures. 15556 belongs to the olivine-normative Apollo 15 suite, in which the compositions of olivine-normative basalts are controlled by olivine growth and fractionation (Ryder and Schuraytz, 2001). Ryder and Schuraytz (2001) found that within this suite bulk compositions can vary on a mm- to cm-scale as a result of the addition or removal of olivine. For example, Sc is generally incompatible in olivine (i.e., K_D<0.5, Beattie, 1994) but generally compatible in pyroxene (i.e., K_D>1.0, Hart and Dunn, 1993), thus initial growth and fractionation of olivine would initially concentrate Sc in the melt. Based on this and the work done here, unique pyroxene Sc may be related to timing of pyroxene crystallization. Grains with relatively elevated Sc contents are not near mesostasis, suggesting that they may have formed early on at a time when melt would have remained Sc-enriched following olivine fractionation. Grains found here to contain low Sc generally border mesostasis

585 on at least one side, and may have crystallized later on. Because core Sc contents form two
586 distinct groups rather than a progressive change, it is possible that pyroxenes crystallized in two-
587 stages, or from a melt that had not efficiently mixed following depletion in Sc as a result of
588 olivine fractionation, likely due to high degrees of undercooling (consistent with plagioclase
589 results). A melt not having effectively homogenized following fractional crystallization is
590 consistent with previous work: Lindstrom and Haskin (1978) determined that compositional
591 changes in the Apollo 15 olivine normative suite resulted from short-range unmixing, where
592 early-formed phases that change the composition of the remaining melt do not effectively
593 fractionate from the melt, thus retaining early-formed grain populations alongside later-formed
594 populations of distinct composition. High degrees of undercooling consistent with this sample's
595 fine-grained nature may have further contributed to preclude efficient element diffusion through
596 melt following olivine growth (e.g., Lofgren et al., 1974, Vernon 2018) and compositional
597 variability in this sample may be the result of closed-system exsolution in diffusively isolated
598 melt pockets.

599 Sample 15556 contains a population of high-Mg olivine macrocrysts, many of which are
600 skeletal (as evidenced by incomplete filling between corner growths, Figs. 3, S3, also irregular
601 growth but not embayment of crystal faces), and some of which are embayed (as evidenced by
602 rounded corners rather than corner growths, Figs. 3, S3). Generally, olivine grains do not
603 otherwise preserve visible reaction textures like those observed in pyroxene via electron
604 microscopy. The olivine macrocrysts are normally zoned, and some host melt inclusions in
605 intermediate growth zones between the core and rim. The cores of olivine in 15556 are all
606 compositionally strikingly similar, but there are two compositionally distinct rim compositions.
607 Cores are defined by Mg# >57.5, 0.47 to 0.26 wt. % Cr_2O_3, and 0.046 to 0.27 wt. % NiO. One

608 rim population is characterized by increasing Cr_2O_3 from core to rim with no significant change
609 in MnO, CaO, or NiO toward the rim (Fig. S12). The second population records normal zoning
610 in Cr_2O_3 core to rim compositions of <0.12 wt. %, and ranges in its degree of compositional
611 change in other elements from core to rim. In some grains CaO remains constant, in others it
612 increases from core values of ~0.2 wt. % to >0.3 wt. % at the rim. The same is true for MnO
613 (~0.3 to ~0.4 wt. % in the core to 0.35-0.75 wt. % in the rim) and NiO (0.02-0.05 wt. % in the
614 core to 0.02 to 0.08 wt. % at the rim). Olivine textures do not correlate with varying rim
615 compositions suggesting that the range of olivine rim compositions stems from diffusion-limited
616 growth for each olivine rather than a sudden change in magma composition due to an event such
617 as magma mixing. Many of the olivine grains record rapid growth as evidenced by skeletal
618 growth at their corners and coincident "bumpy" crystal faces – this is consistent with a degree of
619 rapid undercooling as suggested by previous works (Lofgren, 1974). Additional olivine grains
620 investigated that were not large enough to pursue core-rim analysis via LA-ICP-MS (grains
621 generally <100-150 μm) record a similar range of compositions.

622 ***3.6 Apollo 17 high-Ti basalt 70017***

623 Plagioclase grains in 70017 poikilitically enclose small pyroxene, ilmenite, and olivine
624 grains, and are generally subhedral, ranging from ~0.1 to 2 mm long. Ilmenite records a distinct
625 kink in its CSD (Figs. 4, S2), while the plagioclase feldspar CSD is more complex, recording
626 either multiple kinks in the distribution corresponding to a rapid change in the system, or
627 recording one upwards curve corresponding to crystal accumulation (Fig. 4; e.g., Donohue and
628 Neal, 2015). Compositionally, several grains are variably normally zoned, decreasing by 1 to 5
629 An mol from core to rim; other grains increase only minimally by ~1 An mol from core to rim
630 (Fig. S4). One normal zoned grain has a compositionally distinct core which is notably low in An

631 (An_{79}) and high in FeO_{total} (0.64 wt. %) relative to other cores (>An_{84} ; <0.45 wt. % FeO_{total}), and
632 likely formed at a later stage, as it is also elevated in total REEs (Fig. S6). Two other grains that
633 are reversely zoned in An are elevated in MgO content (>0.3 wt. % at the core and rim) and
634 alkalis (>1.5 wt. % Na_2O+K_2O in the core) relative to others (<0.25 wt. % MgO in cores and
635 rims; <1.5 wt. % Na_2O+K_2O in cores). In the context of trace elements, the normally-An zoned
636 population is also reversely zoned with respect to compatible Eu and Sr (Fig. S5), though in
637 varying amounts (Fig. S5), while the reversely zoned group preserves only minimal change in Eu
638 or Sr content (<0.5 ppm Eu and <30 ppm Sr change from core to rim; Fig. S5). Some grains that
639 are reversely zoned in An and some that are normally zoned in An show an increase in Eu/Eu*
640 from core to rim, while other reversely-zoned grains and normally-zoned grains show a
641 decreasing Eu/Eu* anomaly from core to rim; neither relationship is related to a particular
642 texture. The reverse An zoning is therefore interpreted as a decompression feature (e.g.,
643 Ustunisik et al., 2014) rather than recording a significant change in magma composition
644 (consistent with the lack of a kink in feldspar CSD analysis). While all feldspar grains in this
645 sample are subhedral, the reversely-zoned grains are generally larger (>1.0 mm long) than the
646 normally zoned populations group (<1.0 mm). Due to their larger size, higher MgO content, and
647 decompression features, these grains likely formed earlier and a greater depth in the system prior
648 to transport to a shallower lens. Their REE contents however are not distinct from the normally
649 zoned population (Figs. S6-S7), thus they may reflect crystallization from partial melting of the
650 same source reservoir.

651 Pyroxenes in 70017 are subhedral and poikilitically enclose most of the ilmenite present
652 (Figs. 2-3, 8). Based on dihedral angles, it appears that pyroxenes could have experienced
653 textural coarsening (Higgins 2011), which is consistent with recent work by Gawronska et al.

(2022). Pyroxene zoning is concentric in smaller crystals (<1 mm), but tends to be patchy in the largest grains (>1 mm; Figs. 2, 8). Pyroxenes have cores relatively high in MgO (Mg# > ~63.5), then mantles/overgrowths with ~1 to 3 wt.% increase in MgO and ~400 ppm increase in Cr, and final Fe-rich rims (Mg# <53). Those mantling zones and patches often correspond to sieve textures (Figs. 1-3, 8A, S2). From textural and compositional observations three populations of pyroxene may be present. One population is relatively primitive in composition with elevated Al_2O_3 (>5.9 wt. %), Sc (>120 ppm), V (>200 ppm), Cr (>6000 ppm) in their cores relative to other populations and is interpreted as having crystallized before plagioclase. This population is represented by the largest (> ~1.5 mm) pyroxene grains that record both progressive and patchy zoning (Fig. 8A). A second population is compositionally more evolved. Grain cores are relatively depleted in CaO (<5 wt. %), Sc (<55 ppm), V (<70 ppm), Cr (<3000 ppm), and exhibit lower Dy/Yb values (~1), relative to other cores (Figs. S8-S9). This population is made up of the smallest (generally <0.5 mm), euhedral, concentrically zoned crystals (Fig. 8C). A third population is defined by compositions between these two populations (Figs. 8B, S8-S9), ranging in size from 1.5 mm to 0.5 mm, and generally recording patchy zoning. Because mantling zones of the first population of grains are in textural disequilibrium, these grains likely represent multiple stages of growth in distinct magmatic environments. Three stages of pyroxene growth at different storage locations in the magmatic system are inferred, which is consistent with select plagioclase grains showing storage at depth prior to ascent (as revealed by reverse An zoning that is not coupled with changing plagioclase Sr content). The small, compositionally evolved pyroxenes are reversely zoned in Sc and have distinct core Ce/Y values (Fig. S11), and may represent a wholly distinct magma batch that was encountered by a more primitive melt rising with entrained larger primitive pyroxenes. Resorbed cores of the largest pyroxenes are

677 interpreted as older and antecrystic, eventually being transported by more primitive melt (which
678 imparted sieved mantles that are slightly elevated in MgO, Cr; Figs. S8-S9) to a new location
679 where the compositionally evolved population was encountered, and a new population with
680 intermediate compositions grew. Evolved, small pyroxenes would represent a population that
681 originate from this lens. Prolonged storage in any melt lens, at any stage, explains the textural
682 coarsening documented here and discussed in Gawronska et al. (2022).

683 Olivine in 70017 records a variety of textures depending on grain proximity to late stage
684 mesostasis. Grains shielded from mesostasis retain euhedral to subhedral morphologies, while
685 those bordering on mesostasis record reaction and resorbtion textures including embayment and
686 breakdown into symplectite. This suggests that olivine is generally not in equilibrium with the
687 final melt composition. If interpretations from feldspar and pyroxene elemental stratigraphies are
688 correct, then olivine grains may originate from depth and are reacting with any evolved material
689 incorporated during ascent. Core-to-rim element transects for two olivine grains were completed
690 in this sample. One transect is associated with an olivine enclosed in a pyroxene grain, while the
691 other olivine grains is adjacent to mesostasis and breaking down into symplectite texture (Fig.
692 S3). The enclosed grain maintained near-constant composition from core to rim; for example, it
693 records Mg# of ~69 from core to rim, NiO of 0.014 to 0.013 wt. % from core to rim, Cr_2O_3 from
694 0.20 to 0.18 wt. % from core to rim, and CaO from 0.13 to 0.12 wt. % from core to rim. The
695 grain not enclosed records core composition of Mg# of 66.78 but rim Mg# of 57.46 and is
696 reversely zoned in CaO (from 0.11 to 0.13 wt. %), Cr_2O_3 (from 0.16 to 0.19 wt. %), NiO (from
697 0.010 to 0.040 wt. %), and also in MnO (from 0.44 to 0.41 wt. %). In the context of plagioclase
698 and pyroxene petrogenetic histories, both grains must have begun their growth prior to
699 encountering and reacting with more evolved material. Additional, smaller olivine grains

700 investigated that were not large enough for core-rim investigation record compositions similar to
701 the evolved rim composition of the unenclosed grain.

702 4 Implications for Lunar Magmatic Systems

703 As documented by the pyroxene, feldspar, and olivine crystal populations throughout the
704 samples studied here, Apollo mare basalt crystal cargoes record evidence of interactions between
705 materials of distinct compositions at various stages of magmatic differentiation. Specifically,
706 samples 10057, 12043, 15085, and 70017 contain grains that initially crystallized in
707 compositionally primitive magmatic environments but now coexist with grains that grew in
708 relatively more compositionally evolved melts (i.e., Figs. 5-8). By definition, these types of
709 interactions can only happen in a so-called "open" magmatic system, where material of distinct
710 compositional signatures can be exchanged through a variety of processes (e.g., Davidson et al.,
711 2007; Ginibre et al., 2007; Jerram and Davidson, 2007; Ubide et al., 2014; Ogawa, 2018;
712 Zellmer, 2021). Thus, we have established that the petrogenesis of at least some lunar basalts is
713 associated with open system processes – the possible plumbing system architectures that could
714 have produced the basalts studied here are shown in Fig. 9. We do not find evidence of these
715 processes in samples 12038 or 15556, and thus we will focus on the processes that may have
716 formed 10057, 12043, 15085, and 70017 in the remainder of the work. Nonetheless, samples like
717 12038 and 15556 and the systems from which they originate should be further assessed to better
718 understand the implications of processes operating in closed systems such as convection. While
719 these may be relatively rare on the Moon, such mechanisms would provide further insights into
720 magma dynamics in lunar basaltic systems (i.e., Elardo and Shearer, 2014). To produce distinct
721 batches, magmatic differentiation is inferred to have occurred in distinct lenses within the lunar
722 crust and shallow mantle where magma batches were later remobilized and mixed prior to

723 eventual emplacement on the lunar surface. This work thus also suggests that the architecture of
724 magmatic plumbing systems evolved on the Moon similarly to Earth, and may similarly exist on
725 other bodies where magmatism has operated previously or currently operates, including Mars,
726 Venus, and Jupiter's moon Io (Wilson 2009, and references therein). We identify open magmatic
727 system processes represented by samples from both the low-Ti (12043 and 15085) and high-Ti
728 (10057 and 70017) systems, suggesting these processes may operate in systems across the Moon.
729 Below, we outline the major implications this has for our understanding of magmatic systems on
730 the Moon and beyond.

731 ***4.1 Evaluating the role of crystal mushes***

732 On Earth, it is recognized that some magmatic systems exist as a combination of lenses,
733 some of which are mushy, that can collectively extend vertically throughout the crust (Cashman
734 et al., 2017; Maclennan, 2019; Sparks et al., 2019). These mushes are continuous networks of
735 crystals through which melt is distributed, and in which rheological properties are controlled by
736 the crystalline network, and not the magma (where rheology is controlled by melt; Cashman et
737 al., 2017; Sparks et al., 2019). The transition between these two domains occurs approximately
738 when 30 to 50% melt remains (Sparks et al., 2019). Mushes form when magmas incrementally
739 intrude into the crust, pond in lenses, and solidify over time to form crystal-rich networks (e.g.,
740 Sparks et al., 2019). Recent work on relatively young Chang'e 5 basalts suggests that on the
741 Moon this process could also occur in the lithospheric mantle (Luo et al., 2023), but Weiser et al.
742 (2023) outline the high uncertainty associated with the pressure and temperature estimates of
743 Luo et al. (2023). Mush crystal frameworks are likely variable with respect to their modal
744 proportions, exhibit variation on a centimeter to meter scale (e.g., Lissenberg et al., 2019), and
745 produce igneous crystal cargoes that texturally and chemically trace their magmatic

environment(s) (Solano et al., 2014). Due to the nature of differentiation and distance from mantle source reservoir, lenses which exist deeper within the crust and lithospheric mantle are more likely to be primitive in composition, while upper lenses are more likely to be characterized by more evolved compositions (Cashman et al., 2017; Jackson et al., 2018).

The extensive nature of these magmatic systems stored as a network of mushy lenses allows earliest crystal populations to form at depth, with some later ascending towards the surface as part of a mobilized melt. The evidence for this comes from crystal grains which grow in lower lenses and record relatively primitive compositions in their cores. Those cores can react upon transport and introduction of evolved material, leading to resorbtion, overprinting, and disequilibrium with the host melt. Mineral grains of this simplified history are referred to as antecrysts. Within this framework, there are plagioclase grains in 10057, 12043, 15085, and 70017 that may be antecrystic in nature based on their more primitive compositions, and decompression features indicative of disequilibrium which suggest initial growth occurred prior to transport to a shallower depth. Meanwhile, the pyroxene glomerocryst in 10057, and the pyroxene macrocrysts in 12043, 15085, and 70017 are also antecrysts as evidenced by their disequilibrium textures (Figs. 5-8). This includes resorption in conjunction with changing crystal compositions that correspond to changing melt compositions. These samples also host grains with reverse zoning that correspond to introduction of primitive material which further supports magma assembly from a complex range of primitive and evolved magmas, similar in architecture to some of their terrestrial counterparts. An added implication of mush generation in the lunar setting is a change in melt buoyancy and ascent. As mush crystallization proceeds, the remaining liquid becomes increasingly buoyant and rises via dikes and diapirs, generating new lenses (i.e., Sparks et al., 2019), which is further enhanced through fracturing of brittle crust (i.e., Keller et

769 al., 2013). On the Moon, Wieczorek et al. (2001) proposed that magma buoyancy is the dominant
770 factor in determining whether mare basalts reach the surface, while works like Wilson and Head
771 (2017) found that mare magmas were negatively buoyant everywhere in the crust, and attributed
772 eruptions to excess melt pressures at/below the crust-mantle boundary. In either scenario, mare
773 magma propagation would be enhanced via transport through impact-generated fractures (Spera,
774 1992; Wilson and Head, 2017), but the change in melt buoyancy resulting from mush
775 formation/processing may have further enabled melt ascent on the Moon and would benefit from
776 additional assessment.

777 ***4.2 Melt Transport Through and from a (Mare) Mush***

778 If lunar magmatic systems operated through a network of mushes, melt transport mechanisms
779 must also be further evaluated. In a melt-dominated system, melts can propagate upwards
780 through a network of dikes and sills that are tectonically facilitated (e.g., Lissenberg et al., 2019;
781 Wilding et al., 2023). On the Moon, melt transport could be supported by crustal fracturing as a
782 result of bombardment (Whitford-Stark, 1982). In a system where connected chambers are
783 dominated by mush, it is predicted that melts will migrate through the mush by porous flow over
784 time (McKenzie, 1984; Sparks et al., 2019), or via channelized flow (e.g., Agustsdottir et al.,
785 2015). As crystallization progresses, the melt will either segregate to generate a secondary,
786 separate eruptible melt lens (or chamber), or will become compacted, and will concentrate into
787 highly porous melt layers within the chamber (Solano et al., 2014). The melt layers may then
788 escape upwards due to their buoyancy and establish new lenses at shallower levels, or erupt (e.g.,
789 McKenzie 1984; Lissenberg et al., 2019; Solano et al., 2014; Sparks et al., 2019). In the context
790 of channelized flows, magmatic systems can also be displaced via flow focused in a conduit
791 through a mush, which is a comparatively more rapid process (e.g., Richter and McKenzie, 1984;

792 Lissenberg et al., 2019). This displaced flow may eventually reach the surface during an
793 eruption, driven by the remobilization of otherwise immobile, solidified components (Sparks et
794 al., 2019). Eruption of crystal-containing melt at the surface can be aided by remobilization of
795 materials through heat, potentially as a result of an intrusion at depth or the influx of a hotter,
796 more mafic magma into a storage region. This occurs during mafic recharge which is commonly
797 invoked as a cause for eruptions on Earth (Huber et al., 2011, Lissenberg and MacLeod, 2016;
798 Ubide and Kamber., 2018; Sparks et al., 2019; Gleeson et al., 2023). In particular, eruptions
799 appear to be common in relatively small systems following recharge, though comparatively
800 larger systems may be more buffered against this (Ginibre et al., 2007). Within this framework,
801 the intrusion of hot, primitive magma at depth within a magmatic systems has been shown to be
802 effective at fluidizing crystal mushes, allowing them to rapidly ascend in crystal-poor
803 "chimneys" (Bergantz et al., 2015; Schleicher and Bergantz, 2017; Spera and Bohrson, 2018).

804 *4.2.1 Reactive Flow of Melt in a Mush*

805 As a magma lens continues to evolve and establish a crystal framework, the remaining
806 interstitial melt will become compositionally evolved, and will be in disequilibrium with grains
807 in the network (Lissenberg et al., 2019). Because of this, recent work on terrestrial magmatic
808 systems at mid-ocean ridge settings suggests that melt coexisting with a mush can become
809 reactive (Solano et al., 2014; Lissenberg and MacLeod, 2016; Lissenberg et al., 2019) and move
810 through the mush via reactive flow. Based on compositional modeling of melts at mid-ocean
811 ridge settings, reactive melts can range in composition from primitive (basaltic) to relatively
812 evolved (dacitic) and can thus lead to various interactions with grains in the mush recording
813 highly elevated incompatible element signatures at crystal rims (see discussion by Lissenberg
814 and MacLeod, 2016). Interstitial melts can also become remobilized and mix with any

replenishing melt entering the system via a process like recharge. This leads to the possibility of two reactions: one between the mush framework and the increasingly evolved interstitial melt, and one between the mush framework and any hot, primitive, replenishing magma entering the system (Lissenberg and MacLeod 2016; Lissenberg et al., 2019; Hu et al., 2022). Such interactions cause crystals within the mush to develop dissolution fronts, ragged grain boundaries, symplectites, and compositions distinct from those otherwise predicted by fractional crystallization models, particularly in terms of trace element contents (e.g., Lissenberg and MacLeod, 2016; Hu et al., 2022). The large variety of disequilibrium features observed in terrestrial magmas as a result of reactive flow are reminiscent of the high degree of textural disequilibrium observed in the 15085 pyroxenes (Figs. 3, S3). Pyroxenes in this sample record resorption and in some cases complete breakdown to symplectite, interpreted here as a result of crystal growth at depth, ascent, and stalling in an evolving mushy lens prior to eruption. It is however noted here that the 15085 symplectites are defined by ferrosilite, fayalite, and an Si-rich phase, which is different to the clinopyroxene-amphibole symplectites assemblages observed in terrestrial mid-ocean ridge basalts in which reactive flow studies have primarily been completed (see Lissenberg et al., 2019, and references therein). Such a difference in the reactive mineral assemblage could be a result of the inherent compositional differences between terrestrial and lunar magmas and/or interaction with a more evolved, Fe- and Si-rich reactive melt. Resorption, breakdown, and ragged grain boundaries are also seen in pyroxenes in 70017, and to a lesser degree in 12043. At the time of writing, reactive flow is not fully understood in terrestrial systems, but it has been modeled to occur in a wide variety of magmatic environments (Hu et al., 2022; Gleeson et al., 2023) including on the Moon (Klaver et al., 2024). Reactive flow appears to be a common petrogenetic process operating in terrestrial magma chambers that are mushy in

838 nature, including at ridge settings (e.g., Lissenberg and MacLeod, 2016; Lissenberg et al., 2019;
839 Boulanger et al., 2020) and layered intrusions (e.g., Namur et al., 2013; Leuthold et al., 2014;
840 Maier et al., 2021). On the Moon, reactive flow has been modeled to modify partial melts of
841 ilmenite-bearing cumulates in the lunar mantle into melts resembling erupted high-Ti lavas
842 (Klaver et al., 2024). In this scenario, not only does reactive flow enhance isotopic fractionation
843 of elements such as Mg, Fe, Ca, and Ti, but also decreases melt density allowing high-Ti melts to
844 reach the surface. If true, this process could have influenced the petrogenesis of the high-Ti
845 samples studied here: 10057, and 70017. Thus, future studies investigating extraterrestrial
846 igneous processes should consider the potential role of reactive flow.

847 *4.2.2 Flow of Melt to and from Mush: The Role of Mafic Recharge*

848 Reactive flow can cause melts to rise buoyantly through the crust, and additional
849 mechanisms can work to destabilize this melt further and support remobilization and ascent. In
850 particular, minerals with relatively primitive compositions are too refractory to be dissolved and
851 unlocked by more evolved melts (Neave et al., 2014; Ubide and Kamber, 2018), but relatively
852 evolved grains can be more easily entrained from pre-existing shallower zones (e.g., Ganne et
853 al., 2018). Mafic recharge is a particularly effective mechanism for defrosting, unlocking, and
854 destabilizing mush and interstitial melt (Huber et al., 2011, Lissenberg and MacLeod, 2016,
855 Sparks et al., 2019; Gleeson et al., 2023). Any intruding primitive hot magma mixes with
856 interstitial melt and reacts with framework grains, unlocking them. By mixing with interstitial
857 melt and (partially) dissolving framework grains, magma influx leads to homogenization of the
858 melts ultimately derived from mushy lenses and erupted at the surface (e.g., Lissenberg et al.,
859 2019). By unlocking mushes, a replenishing melt traveling through several lenses also has the
860 potential to entrain diverse populations of phenocrysts and glomerocrysts (e.g., Cashman et al.,

2017; Ubide and Kamber, 2018; Lissenberg et al., 2019). Dissolution of grains as a result of (mafic) recharge is also commonly recognized as a process through which disequilibrium features can be generated (e.g., Ubide and Kamber., 2018). Introduction of primitive, hot magma carries with it a relative influx of MgO and Cr (for example) and can be coupled with disequilibrium features like resorption/dissolution. These textural and chemical features are observed in this study particularly with increased MgO and Sr contents in feldspar populations from core to rim, and increased MgO, Cr, and Sc from core to mantle/rim coupled with dissolution and sieving clearly seen in pyroxenes. Thus, it is inferred that mafic recharge was also an important process in the evolution of lunar magmatic systems and should be investigated further as a potential eruption trigger in extraterrestrial settings.

5 Conclusions

Through a detailed, coupled textural and chemical study of lunar basalt crystal cargoes, this work indicates that multiple lunar magmatic systems are more complex than previously recognized (irrespective of Ti content). Collectively, CSD profiles, disequilibrium textures, and variations in major, minor, and trace elements chemistries record distinct petrogenetic histories at the crystal scale in lunar basalts. This is not unlike terrestrial basaltic counterparts. This suggests that magmatic plumbing system architecture evolves similarly across rocky planetary bodies, and may operate similarly on other bodies where magmatism has operated previously or currently operates, including Mars, Venus, and Jupiter's moon Io (Wilson, 2009, and references therein; see Fig. 9). The depths at which these processes occur likely differ across planetary objects due to their unique rheological properties. On Earth, magmatic system lenses form transcrustal systems, but the recent work of Luo et al. (2023) on pyroxene petrogenesis in young (~2 Ga) basaltic Chang'e 5 samples may indicate magmatic differentiation occurred in the lunar

lithosphere. Detailed, multi-sample investigations of each of the six magmatic systems studied here are recommended, along with detailed evaluations of other mare basalt suites, with the consideration of melt transport and storage processes (e.g., mushes and reactive flow). Finally, basaltic samples from other planetary objects should be studied within this framework in order to fully determine how plumbing system architecture and processes influence basaltic magma petrogenesis across the Solar System.

6 Acknowledgements

First, we acknowledge the Apollo astronauts for collecting the lunar samples studied here, and all those involved in the Apollo program who made this possible. We also extend our thanks to M. Duley at the Miami University Center for Advanced Microscopy and Imaging (CAMI) for his support during sample imaging, and M. Gillis from the Miami University Department of Geology and Environmental Earth Science for help in carbon coating sample thin sections. Finally, we thank D. Neave and an anonymous reviewer for their thorough and constructive feedback which greatly helped to improve this manuscript. We acknowledge the editors of this special publication for their work in generating this volume that illuminates contributions to planetary science by early-career researchers. This research was funded through a 2021 Geological Society of America Graduate Student Research Grant #13203-21 to AJG.

7 Data Availability

Data is made available via a repository, see Gawronska (2025).

8 References

1. Ágústsdóttir, T., Woods, J., Greenfield, T., Green, R. G., White, R. S., Winder, T., Brandsdóttir, B., et al. (2016) Strike-slip faulting during the 2014 Bárðarbunga-Holuhraun dike

intrusion, central Iceland. Geophysical Research Letters 43:4, 1495-1503. https://doi.org/10.1002/2015GL067423

2. Basaltic Volcanism Study Project (BVSP) (1981) Basaltic Volcanism on the Terrestrial Planets. Pergamon Press, Inc., New York. 1286 pp.
3. Beattie, P. (1994) Systematics and energetics of trace-element partitioning between olivine and silicate melts: Implications for the nature of mineral/melt partitioning. Chemical Geology 117, 57-71.
4. Bennett, E. N., Lissenberg, C. J., Cashman, K. V. (2019) The significance of plagioclase textures in mid-ocean ridge basalt (Gakkel Ridge, Arctic Ocean). Contributions to Mineralogy and Petrology 174: 49. https://doi.org/10.1007/s00410-019-1587-1
5. Berlo, K., Blundy, J., Turner, S., Hawkesworth, C., 2007. Textural and chemical variation in plagioclase phenocrysts from the 1980 eruptions of Mount St. Helens, USA. Contrib. Mineral. Petrol. 154, 291–308.
6. Bergantz et al., 2015
7. Bezard, R., Turner, S., Davidson, J., Schmitt, A.K., Lindsay, J., 2017. Origin and Evolution of Silicic Magmas in Oceanic Arcs; an in situ Study from St Lucia, Lesser Antilles. J. Petrol.58, 1279–1318.
8. Blundy J. D., Shimizu N. (1991) Trace element evidence for plagioclase recycling in calcalkaline magmas. Earth and Planetary Science Letters 102:2, 178-197.
9. Blundy, J. D., Wood, B. J. (1991) Crystal-chemical controls on the partitioning of Sr and Ba between plagioclase feldspar, silicate melts, and hydrothermal solutions. Geochimica et Cosmochimica Acta 55, 193-209.

10. Boulanger, M., France, L., Deans, J. R. L., Ferrando, C., Lissenberg, C. J., von der Handt, A. (2020) Magma reservoir formation and evolution at a slow-spreading center (Atlantis Bank, Southwest Indian Ridge). Frontiers in Earth Science 8, https://doi.org/10.3389/feart.2020.554598
11. Cashman K. V. (2015) Changing the paradigm – new views on magmatic systems provide new perspectives on volcanic processes. AGU, Fall Meeting 2015.
12. Cashman K. V., Sparks R. S. J., Blundy J. D. (2017) Vertically extensive and unstable magmatic systems: A unified view of igneous processes. Science 355, 6331. https://doi.org/10.1126/science.aag3055
13. Coish, R. A., Taylor, L. A. (1979) The Effects of Cooling Rate on Texture and Pyroxene Chemistry in DSDP LEG 34 Basalt: A Microprobe Study. Earth and Planetary Science Letters 42, 389-398.
14. Coote, A., Shane, P. (2018) Open-system magmatic behaviour beneath monogenetic volcanoes revealed by the geochemistry, texture and thermobarometry of clinopyroxene, Kaikohe-Bay of Islands volcanic field (New Zealand). Journal of Volcanology and Geothermal Research 368, 51-62. https://doi.org/10.1016/j.jvolgeores.2018.11.006
15. Costa, F., Morgan, D. (2011) Time Constraints from Chemical Equilibration in Magmatic Crystals. In: Dosseto, A., Turner, S. P., Van Orman, J. A. (Eds.) Timescales of Magmatic Processes: From Core to Atmosphere. Blackwell Publishing Ltd.
16. Couperthwaite, F. K., Thordarson, T., Morgan, D. J., Harvey, J., Wilson, M. (2020) Diffusion Timescales of Magmatic Processes in the Moinui Lava Eruption at Mauna Loa, Hawai'I, as Inferred from Bimodal Olivine Populations. Journal of Petrology 61 (7), egaa058. https://doi.org/10.1093/petrology/egaa058

17. Davidson J. P., Morgan D. J., Charlier B. L. A., Harlou R., Hora J. M. (2007) Microsampling and Isotopic Analysis of Igneous Rocks: Implications for the Study of Magmatic Systems. Annual Reviews in Earth and Planetary Science 35, 273-311. https://doi.org/10.1146/annurev.earth.35.031306.140211

18. Donohue P. H., Neal C. R. (2015) Quantitative textural analysis of ilmenite in Apollo 17 high titanium mare basalts. Geochimica et Cosmochimica Acta 149, 115-130. https://doi.org/10.1016/j.gca.2014.11.002

19. Edmonds, M., Cashman, K. V., Holness, M., Jackson, M. (2019) Architecture and dynamics of magma reservoirs. Philosophical Transactions of the Royal Society A, 377: 20180298. http://dx.doi.org/10.1098/rsta.2018.0298

20. Elardo, S. M., Shearer, C. K. (2014). Magma chamber dynamics recorded by oscillatory zoning in pyroxene and olivine phenocrysts in basaltic lunar meteorite Northwest Africa 032. American Mineralogist, 99, 355-368. https://doi.org/10.2138/am.2014.4552

21. Gaffney, A. M., Gross, J., Borg, L. E., Donaldson Hanna, K. L., Draper, D. S., Dygert, N., Elkins-Tanton, L. T., Prissel, K. B., Prissel, T. C., Steenstra, E. S., van Westrenen, W. (2023) Magmatic evolution I: Initial differentiation of the Moon. In: Neal, C. R., Gaddis, L. R., Jolliff, B. L., Lawrence, S. J., Mackwell, S. J., Shearer, C. K., Valencia, S. N, eds., New Views of the Moon 2. Reviews in Mineralogy and Geochemistry 89 (1), 147–206. https://doi.org/10.2138/rmg.2023.89.04

22. Gawronska, A. J., McLeod, C. L., Blumenfeld, E. H., Hanna, R. D. Zeigler, R. A. (2022) New interpretations of lunar mare basalt flow emplacement from XCT analysis of Apollo samples. Icarus 388, 115216. https://doi.org/10.1016/j.icarus.2022.115216.

23. [dataset] Gawronska, A. (2025), “Evidence for open magmatic system processes recorded in crystal cargoes of lunar basalts”, Mendeley Data, V1, https://doi.org/10.17632/b49p7nc792.1
24. Ginibre C., Worner G., Kronz A. (2007) Crystal Zoning as an Archive for Magma Evolution. Elements 3, 261-266. https://doi.org/10.2113/gselements.3.4.261
25. Gleeson, M. L. M., Lissenberg, C. J., Antoshechkina, P. M. (2023) Porosity evolution of mafic crystal mush during reactive flow. Nature Communications 14, 2088. https://doi.org/10.1038/s41467-023-38136-x
26. Grove, T. L., Baker, M. B., Kinzler, R. J. (1984) Coupled CaAl-NaSi diffusion in plagioclase feldspar: Experiments and applications to cooling rate speedometry. Geochimica et Cosmochimica Acta 48, 2113-2121.
27. Grove, T. L., Bence, A. E. (1977) Experimental study of pyroxene-liquid interaction in quartz-normative basalt 15597. Proceedings of the 8th Lunar Science Conference, 1549-1579.
28. Grove, T. L., Juster, T. C. (1989) Experimental investigations of low-Ca pyroxene stability and olivine – pyroxene – liquid equilibria at 1-atm in natural basaltic and andesitic liquids. Contributions to Mineralogy and Petrology 103, 287-305. https://doi.org/10.1007/BF00402916
29. Hart, S. R., Dunn, T. (1993) Experimental cpx/melt partitioning of 24 trace elements. Contributions to Mineralogy and Petrology 113, 1-8.
30. Head, J. W., (1976) Lunar volcanism in space and time. Reviews of Geophysics 14 (2), 265-300.
31. Higgins M. D. (2000) Measurement of crystal size distributions. American Mineralogist 85, 1105-1116. https://doi.org/10.2138/am-2000-8-901

995 32. Higgins M. D., Roberge J. (2007) Three magmatic components in the 1973 eruption of Eldfell
996 volcano, Iceland: Evidence form plagioclase crystal size distribution (CSD) and geochemistry.
997 Journal of Volcanology and Geothermal Research 161:3, 247-60.
998 https://doi.org/10.1016/j.jvolgeores.2006.12.002
999 33. Hu, H., Jackson, M. D., Blundy, J. (2022) Melting, Compaction, and Reactive Flow: Controls
1000 on Melt Fraction and Composition Change in Crustal Mush Reservoirs. (2022) Journal of
1001 Petrology 63 (11), egac097. https://doi.org/10.1093/petrology/egac097
1002 34. Jackson M, Blundy J, Sparks RSJ. 2018 Chemical differentiation, cold storage and
1003 remobilization of magma in the Earth's crust. Nature 355, eaag3055. doi:10.1038/s41586-018-
1004 0746-2
1005 35. Jerde E. A., Snyder G. A., Taylor L. A., Liu Y.-G., Schmitt R. A. (1994) The origin and
1006 evolution of lunar high-Ti basalts: Periodic melting of a single source at Mare Tranquilitatis.
1007 Geochimica et Cosmochimica Acta 58, 515-527. https://doi.org/10.1016/0016-
1008 7037(94)90480-4
1009 36. Jerram D. A., Davidson J. P. (2007) Frontiers in Textural and Microgeochemical Analysis.
1010 Elements 3:4, 235-238. https://doi.org/10.2113/gselements.3.4.235
1011 37. Kent, A. J. R., Darr, C., Koleszar, A. M., Salisbury, M. J., Cooper, K. M. (2010) Preferential
1012 eruption of andesitic magmas through recharge filtering. Nature Geoscience 3, 631-636.
1013 https://doi.org/10.1038/ngeo924
1014 38. Keller, T., May, D. A., Kaus, B. J. P. (2013). Numerical modelling of magma dynamics
1015 coupled to tectonic deformation of lithosphere and crust. Geophysical Journal International
1016 195(3), 1406–1442. https://doi.org/10.1093/gji/ggt306
1017 39. Klaver, M., Klemme, S., Liu, X.-N., Hin, R. C., Coath, C. D., Anand, M., Lissenberg, C. J.,
1018 Berndt, J., Elliott, T. (2024). Titanium-rich basaltic melts on the Moon modulated by reactive

flow processes. Nature Geoscience, 17(2), 118-123. https://doi.org/10.1038/s41561-023-01362-5

40. Lee C-T. A., Luffi P., Plank T., Dalton H., Leeman W. P. (2009) Constraints on the depths and temperatures of basaltic magma generation on Earth and other terrestrial planets using new thermobarometers for mafic magmas. Earth and Planetary Science Letters 279:1-2, 20-33. https://doi.org/10.1016/j.epsl.2008.12.020

41. Leuthold, J., Blundy, J. D., Holness, M. B., Sides, R. (2014) Successive episodes of reactive liquid flow through a layered intrusion (Unit 9, Rum Eastern Layered Instrusion, Scotland). Contributions to Mineralogy and Petrology 168, 1021. https://doi.org/10.1007/s00410-014-1021-7

42. Lindstrom, M. M., Haskin, L. A. (1978) Causes of compositional variations within mare basalt suites. Proceedings of the 9th Lunar and Planetary Science Conference, 465-486.

43. Lissenberg, C. J., MacLeod, C. J. (2016) A Reactive Porous Flow Control on Mid-ocean Ridge Magmatic Evolution. Journal of Petrology 57 (11&12), 2195-2220. https://doi.org/10.1093/petrology/egw074

44. Lissenberg, C. J., MacLeod, C. J., Bennett, E. N. (2019) Consequences of a crystal mush-dominated magma plumbing system: a mid-ocean ridge perspective. Philosophical Transactions of the Royal Society A 377: 20180014. http://dx.doi.org/10.1098/rsta.2018.0014

45. Lofgren, G., Donaldson, C. H., Williams, R. J., Mullins Jr., O., Usselman, T. M. (1974) Experimentally reproduced textures and mineral chemistry of Apollo 15 quartz normative basalts. Proceedings of the Fifth Lunar Conference 5 (1), 549-567.

46. Luo, B., Wang, Z., Song, J., Qian, Y., He, Q., Li, Y., Head, J. W., et al. (2023) The magmtic architecture and evolution of the Chang'e-5 lunar basalts. Nature Geoscience 16, 301-308. https://doi.org/10.1038/s41561-023-01146-x

47. Maclennan, J. 2019. Mafic tiers and transient mushes: evidence from Iceland. Philosophical Transactions of the Royal Society A 377, 20180021. http://doi.org/10.1098/rsta.2018.0021

48. Maier, W. D., Barnes, S.-J., Muir, D., Savard, D., Lahaye, Y., Smith, W. D. (2021) Formation of Bushveld anorthosite by reactive porous flow. Contributions to Mineralogy and Petrology 176(3). https://doi.org/10.1007/s00410-020-01760-7

49. Marsh B. D. (2009) Dynamics of Magmatic Systems. Elements 2:5, 287-292. https://doi.org/10.2113/gselements.2.5.287

50. McKenzie, D. (1984) The Generation and Compaction of Partially Molten Rock. Journal of Petrology 25 (3), 713-765.

51. McLeod, C. L., Gawronska, A. J. (2023) The Lunar Mantle. In: Cudnik, B. (Eds.) Encyclopedia of Lunar Science. Springer, Cham. https://doi.org/10.1007/978-3-319-14541-9_213

52. Meyer, C., 2016. The Lunar Sample Compendium Database. Astromaterials Research and Exploration Science. https://curator.jsc.nasa.gov/lunar/lsc/

53. Middlemost E. A. K. (2014) Magmas, Rocks and Planetary Development. Routlege, London. 324 pp

54. Mollo, S., Putirka, K., Iezzi, G., Del Gaudio, P., Scarlato, P. (2011) Plagioclase-melt (dis)equilibrium due to cooling dynamics: Implications for thermometry, barometry, and hygrometry. Lithos 125, 221-235. doi:10.1016/j.lithos.2011.02.008

55. Moore, A., Coogan, L. A., Costa, F., Perfit, M. R. (2014) Primitive melt replenishment and crystal-mush disaggregation in the weeks preceding the 2005-2006 eruptions 9º50'N, EPR. Lithos 403 (15-26). https://doi.org/10.1016/j.epsl.2014.06.015

56. Morgan D. J., Jerram D. A. (2006) On estimating crystal shape for crystal size distribution analysis. Journal of Volcanology and Geothermal Research 154, 1-7. https://doi.org/10.1016/j.jvolgeores.2005.09.016

57. Namur, O., Humphreys, M. C. S., Holness, M. B. (2013) Lateral reactive infiltration in a vertical gabbroic crystal mush, Skaergaard Intrusion, East Greenland. Journal of Petrology 54(5), 985-1016. https://doi.org/10.1093/petrology/egt003

58. National Research Council (2007) The Scientific Context for Exploration of the Moon. Washington, DC: The National Academies Press. https://doi.org/10.17226/11954.

59. Neal, C. R., Taylor L. A. (1992) Petrogenesis of mare basalts: A record of lunar volcanism. Geochimica et Cosmochimica Acta 56, 2177-2211.

60. Neal, C. R., Hacker, M. D., Snyder, G. A., Taylor, L. A., Liu, Y.-G., Schmitt , R. A. (1994) Basalt generation at the Apollo 12 site: Part 1: New data, classification, and re-evaluation. Meteoritics 29, 334-348

61. Neal C. R., Donohue P., Fagan A. L., O'Sullivan K., Oshrin J., Roberts S. (2015) Distinguishing between basalts produced by endogenic volcanism and impact processes: A non-destructive method using quantitative petrography of lunar basaltic samples. Geochimica et Cosmochimica Acta 148, 6280. https://doi.org/10.1016/j.gca.2014.08.020

62. Neave, D. A., Maclennan, J., Hartley, M. E., Edmonds, M. & Thordarson, T. (2014) Crystal storage and transfer in basaltic systems: the Skuggafjöll eruption, Iceland. J. Petrol. 55, 2311–2346

63. Neave, D. A., Maclennan J. (2020) Clinopyroxene Dissolution Records Rapid Magma Ascent. Frontiers in Earth Science 8, 188. https://doi.org/10.3389/feart.2020.00188

64. Neave, D. A., Beckmann, P., Behrens, H., Holtz, F. (2021) Mixing between chemically variable primitive basalts creates and modifies crystal cargoes. Nature Communications 12, 5492. https://doi.org/10.1038/s41467-021-25820-z

65. Nyquist, L. E., Wooden, J. L., Shih, C.-Y., Wiesmann, H., Bansal, B. M. (1981) Isotopic and REE studies of lunar basalt 12038: implications for petrogenesis of aluminous mare basalts. Earth and Planetary Science Letters 55, 335-355.

66. Ogawa M. (2018) Magmatic differentiation and convective stirring of the mantle in early planets: the effects of the magmatism-mantle upwelling feedback. Geophysical Journal International 215:3, 2144-2155. https://doi.org/10.1093/gji/ggy413

67. Paces, J. B., Nakai, S., Neal, C. R., Taylor, L. A., Halliday, A. N., Lee, D.-C. (1991) A strontium and neodymium isotopic study of Apollo 17 high-Ti mare baslts: Resolution of ages, evolution of magmas, and origins of source heterogeneities. Geochimica et Cosmochimica Acta 55, 2025-2043.

68. Papike, J. J., Hodges, F. N., Bence, A. E., Cameron, M., Rhodes, J. M. (1976) Mare Basalts: Crystal Chemistry, Mineralogy, and Petrology. Reviews of Geophysics and Space Physics 14 (4), 475-540.

69. Paulatto, M., Hooft, E. E., Chrapkiewicz, K., Heath, B., Toomey, D. R., Morgan, J. V. (2022) Advances in seismic imaging of magma and crystal mush. Frontiers in Earth Science 10. https://doi.org/10.3389/feart.2022.970131

70. Qian, Y., Xiao, L., Wang, Q., Head, J. W., Yang, R., Kang, Y., van der Bogert, C. H., Hiesinger, H., Lai, X., Wang, G., Pang, Y., Zhang, N., Yuan, Y., He, Q., Huang, J., Zhao, J.,

Wang, J., Zhao, S. (2021) China;s Chang'e-5 landing site: Geology, stratigraphy, and provenance of materials. Earth and Planetary Science Letters 561, 116855. https://doi.org/10.1016/j.epsl.2021.116855

71. Richter F. M., McKenzie D. (1984) Dynamical models for melt segregation from a deformable matrix. J. Geol. 92, 729–740. https://doi.org/10.1086/628908

72. Ross, M., Bence, A. E., Dwornik, E. J., Clark, J. R., Papike, J. J. (1970) Mineralogy of the lunar clinopyroxenes, augite and pigeonite. Proceedings of the Apollo 11 Lunar Science Conference 1, 839-848.

73. Ryder, G., Schuraytz, B. C. (2001) Chemical variation of the large Apollo 15 olivine-normative mare basalt rock samples. Journal of Geophysical Research 106 (E1), 1435-1451.

74. Salisbury, M. J., Bohrson, W. A., Clynne, M. A., Ramos, F. C., Hoskin, P. (2008) Multiple Plagioclase Crystal Populations Identified by Crystal Size Distribution and *in situ* Chemical Data: Implications for Timescales of Magma Chamber Processes Associated with the 1915 Eruption of Lassen Peak, CA. Journal of Petrology 49 (10), 1755-1780. https://doi.org/10.1093/petrology/egn045

75. Schleicher J, Bergantz G. (2017) The mechanics and temporal evolution of an open-system magmatic intrusion into a crystal-rich magma. J. Petrol. 58, 1059–1072. https://doi.org10.1093/petrology/egx045

76. Schneider, C. A., Rasband, W. S., Eliceiri, K. W., (2012). NIH Image to ImageJ: 25 years of image analysis. Nature methods 9(7), 671-675, https://doi.org/10.1038/nmeth.2089

77. Shearer, C. K., Hess, P. C., Wieczorek, M. A., Pritchard, M. E., Parmentier, E. M., Borg, L. E., Longhi, J., Elkins-Tanton, L. T., Neal, C. R., Antonenko, I., Canup, R. M., Halliday, A. N., Grove, T. L., Hager, B.H., Lee, D-C., Wiechert, U., (2006) Thermal and Magmatic

Evolution of the Moon, in: Jollif, B. L., Wieczorek, M. A., Shearer, C. K., Neal, C. R., eds., New Views of the Moon. Reviews in Mineralogy & Geochemistry 60(1), 365-518, https://doi.org/10.2138/rmg.2006.60.4

78. Shearer, C., Neal, C. R., Glotch, T. D., Prissel, T. C., Bell, A. S., Fernandes, V. A., Gaddis, L. R., Jolliff, B. L., Laneuville, M., Magna, T., Simon, J. (2023) Magmatic evolution II: A new view of post-differentiation magmatism. In: Neal, C. R., Gaddis, L. R., Jolliff, B. L., Lawrence, S. J., Mackwell, S. J., Shearer, C. K., Valencia, S. N, eds., New Views of the Moon 2. Reviews in Mineralogy and Geochemistry 89 (1), 147–206. https://doi.org/10.2138/rmg.2023.89.04

79. Shen, D., Li, S., Li, S., Xu, Y., Li, Y., Li, M., Wang, D., Pang, R., Zhang, Y., Han, Z. (2025) Petrogenesis of Chang'E-6 basalts and implication for multi-episode volcanism in the lunar farside basin. Earth and Planetary Science Letters 659, 119335. https://doi.org/10.1016/j.epsl.2025.119335

80. Snape, J. F., Nemchin, A. A., Whitehouse, M. J., Merle, R. E., Hopkinson, T., Anand, M. (2019) The timing of basaltic volcanism at the Apollo landing sites. Geochimica et Cosmochimica Acta 266, 29-53. https://doi.org/10.1016/j.gca.2019.07.042

81. Solano, J. M. S., Jackson, M. D., Sparks, R. S. J., Blundy, J. (2014) Evolution of major and trace element composition during melt migration through crystalline mush: Implications for chemical differentiation in the crust. American Journal of Science 314 (5), 895-939. https://doi.org/10.2475/05.2014.01

82. Sparks, R. S. J., Annen, C., Blundy, J. D., Cashman, K. V., Rust, A. C., Jackson, D. (2019) Formation and dynamics of magma reservoirs. Philosophical Transactions of the Royal Society A 377, 20180019. http://dx.doi.org/10.1098/rsta.2018.0019

1154 83. Spera, F. J. (1992) Lunar magma transport phenomena. Geochimica et Cosmochimica Acta
1155 56(6), 2253-2265. https://doi.org/10.1016/0016-7037(92)90187-N
1156 84. Spera, F. J., Bohrson, W. A. (2018) Rejuvenation of crustal magma mush: A tale of multiply
1157 nested processes and timescales. American Journal of Science 318 (1), 90-140.
1158 https://doi.org/10.2475/01.2018.05
1159 85. Spudis, P. D., McGovern, P. J., Kiefer, W. S. (2013) Large shield volcanoes on the Moon.
1160 Journal of Geophysical Research: Planets 118 (5), 1063-1081.
1161 https://doi.org/10.1002/jgre.20059
1162 86. Stooke, P. J. (2017) Luna Missions. In: Cudnik, B. (eds) Encyclopedia of Lunar Science.
1163 Springer, Cham. https://doi.org/10.1007/978-3-319-05546-6_97-1
1164 87. Streck, M. J. (2008) Mineral Textures and Zoning as Evidence for Open System Processes.
1165 Reviews in Mineralogy and Geochemistry 69, 595-622.
1166 https://doi.org/10.2138/rmg.2008.69.15
1167 88. Sun, S.-s., McDonough, W. F. (1989) Chemical and isotopic systematics of oceanic basalts:
1168 implications for mantle composition and processes. In: Saunders, A. D., Norry, M. J. (Eds.)
1169 Magmatism in the Ocean Basins. Geological Society Special Publications 42, 313-345 pp.
1170 89. Ubide T., Gale C., Larrea P., Arranz E., Lago M., Tierz P. (2014) The Relevance of Crystal
1171 Transefer to Magma Mixing: A Case Study in Composite Dykes from the Central Pyrenees.
1172 Journal of Petrology 55:8, 1535-1559. https://doi.org/10.1093/petrology/egu033
1173 90. Ubide, T., Kamber, B. S. (2018) Volcanic crystals as time capsules of eruption history. Nature
1174 Communications 9: 326. https://doi.org/10.1038/s41467-017-02274-w
1175 91. Ubide, T., Caulfield, J., Brandt, C., Bussweiler, Y., Mollo, S., Di Stefano, F., Nazzari, M.,
1176 Scarlato, P. (2019) Deep Magma Storage Revealed by Multi-Method Elemental Mapping of

Clinopyroxene Megacrysts at Stromboli Volcano. Frontiers in Earth Science 7:239. https://doi.org/10.3389/feart.2019.00239

92. Ustunisik, G., Kilinc, A., Nielsen, R. L. (2014) New insights into the processes controlling compositional zoning in plagioclase. Lithos 200-201, 80-93. http://dx.doi.org/10.1016/j.lithos.2014.03.021

93. Velázquez Santana, L. C., McLeod, C. L., Blakemore, D., Shaulis, B., Hill, T. (2020) Bolivian hornblendite cumulates: Insights into the depths of Central Andean arc magmatic systems. Lithos 370-371, 105618. https://doi.org/10.1016/j.lithos.2020.105618

94. Vernon, R. H., 2018. A Practical Guide to Rock Microstructure, 2nd edition. Cambridge University Press, Cambridge. doi: 10.1017/9781108654609

95. Vetter, S. K., Shervais, J. W., Lindstrom, M. M. (1988) Petrology and Geochemistry of Olivine-Normative and Quartz-Normative Basalts from Regolith Breccia 15498: New Diversity in Apollo 15 Mare Basalts. Proceedings of the 18th Lunar and Planetary Science Conference.

96. Wieser, P. E., Till, C., Kent, A. Gleeson, M. (2023) Comment on 'The magmatic architecture and evolution of the Chang'e-5 lunar basalts.' Earth ArXiv preprint. https://doi.org/10.31223/X5MM3B

97. Whitford-Stark, J. L. (1982) Factors influencing the morphology of volcanic landforms: An earth-moon comparison. Earth-Science Reviews 18 (2), 109-168. https://doi.org/10.1016/0012-8252(82)90050-2

98. Wieczorek, M. A., Zuber, M. T., Phillips, R. J. (2001) The role of magma buoyancy on the eruption of lunar basalts. Earth and Planetary Science Letters 185(1-2), 71-83. https://doi.org/10.1016/S0012-821X(00)00355-1

99. Wilding, J. D., Zhu, W., Ross, Z. E., Jackson, J. M. (2023) The magmatic web beneath Hawai'i. Science 379, 462-468. https://doi.org/10.1126/science.ade5755

100. Wilson, L. (2009) Volcanism in the Solar System. Nature Geoscience 2, 389-397. https://doi.org/10.1038/ngeo529

101. Wilson, L., Head, J. W. (2017) Generation, ascent and eruption of magma on the Moon: New insights into source depths, magma supply, intrusions and effusive/explosive eruptions (Part 1: Theory). Icarus 283, 146-175. https://doi.org/10.1016/j.icarus.2015.12.039

102. Xue, Z., Welsh, D. F., Neal, C. R., Xiao, L. (2021) Understanding the textures of Apollo 11 high-Ti mare basalts: A quantitative petrographic approach. Meteoritics and Planetary Science 56(12) 2211-2229. https://doi.org/10.1111/maps.13767

103. Yang, H. and Zhao, W. (2018) Apollo Program. In: Cudnik, B. (eds) Encyclopedia of Lunar Science. Springer, Cham. https://doi.org/10.1007/978-3-319-05546-6_101-1

104. Zellmer, G. (2021) Gaining acuity on crystal terminology in volcanic rocks. Bulletin of Volcanology 83:77. https://doi.org/10.1007/s00445-021-01505-9

105. Zhou, Q. (2017) Lunar Meteorites. In: Cudnik, B. (Eds.) Encyclopedia of Lunar Science. Springer, Cham. https://doi.org/10.1007/978-3-319-05546-6_58-1

1218 **9. Figure**

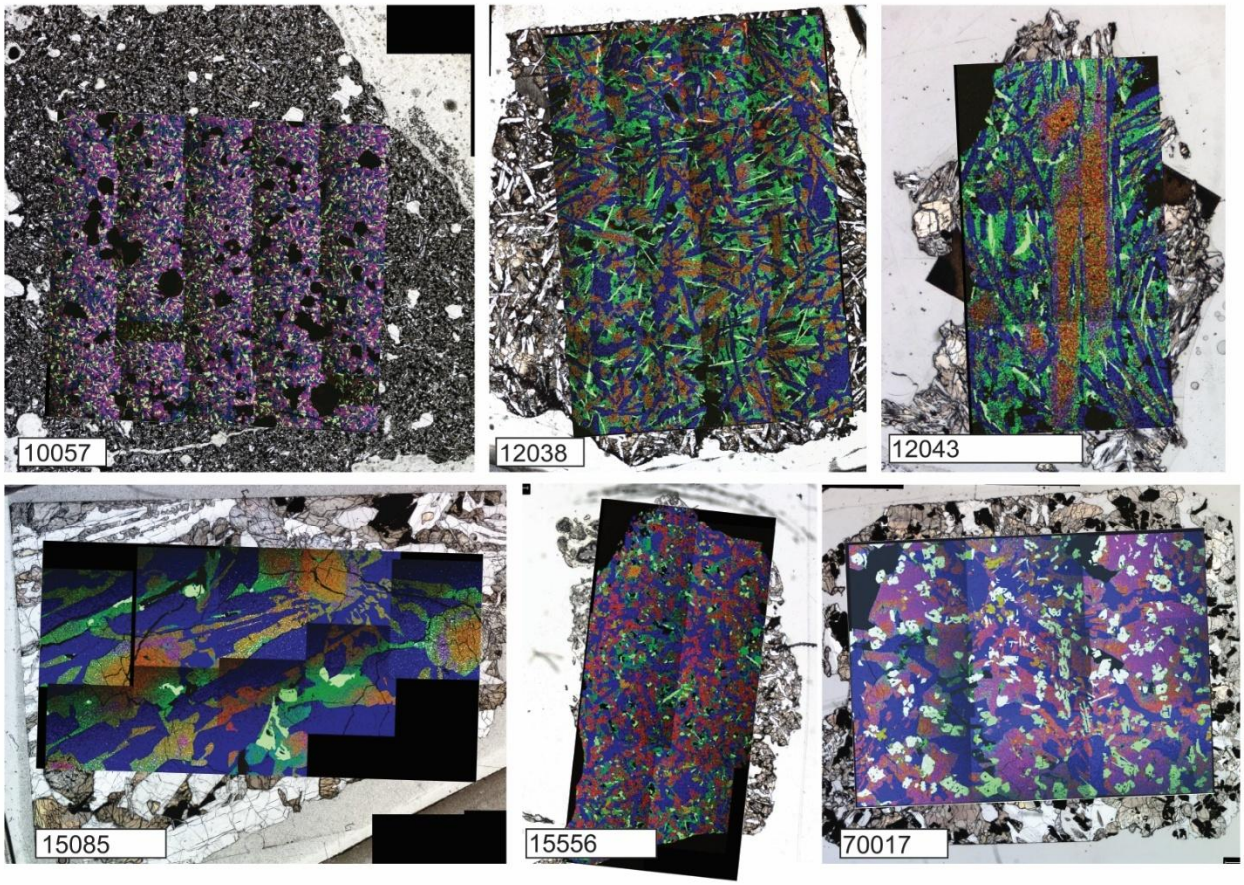

1219
1220 **s**
1221

Fig. 1: Schematic of crystal zoning patterns resulting from diverse processes operating in open systems as a result of compositional change. Autocrystic grains can preserve normal and progressive zoning, and/or resorption/dissolution due to changes in melt composition (e.g., Davidson et al., 2007; Jerram et al., 2018; Zellmer, 2021). Phenocrystic populations are expected to preserve normal compositional zoning, while xenocrystic populations can have complex histories (e.g., Zellmer, 2021). Note that physical change like decreasing pressure and depth can generate additional changes in zoning as a result of decompression-induced dissolution (i.e., dissolution of An in plagioclase feldspar, Ustunisik et al., 2014).

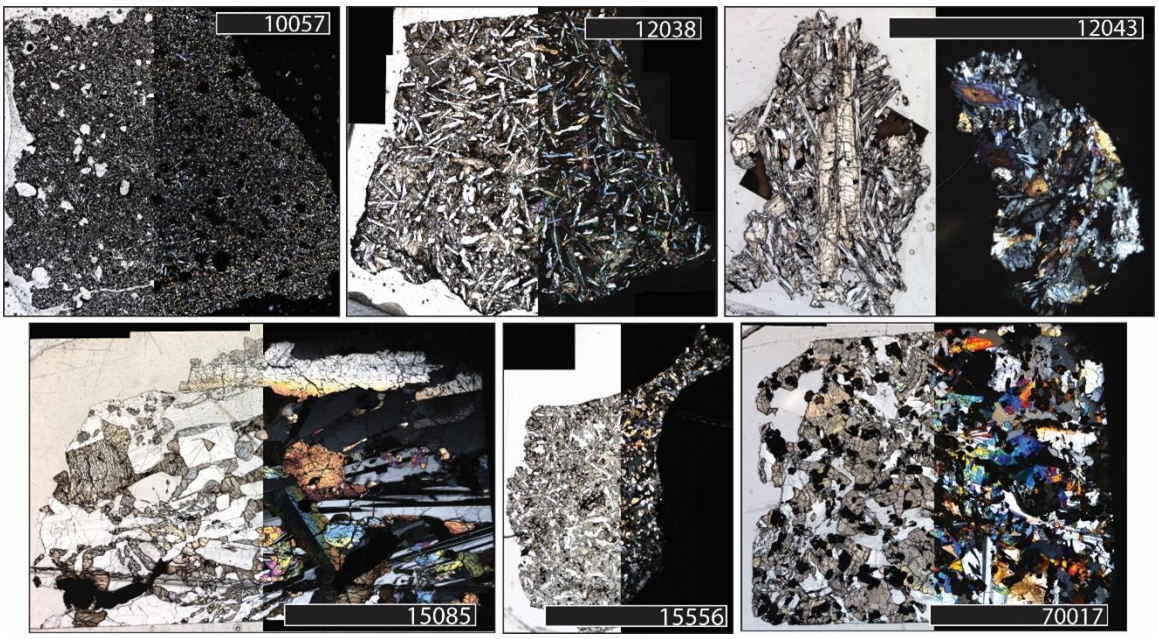

Fig. 2: Photomicrographs of representative thin sections in plane polarized light (left) and cross polarized light (right) for each sample. Scalebars are 5 mm. SEM-EDS maps of each sample in the same field of view are provided in Figure S1.

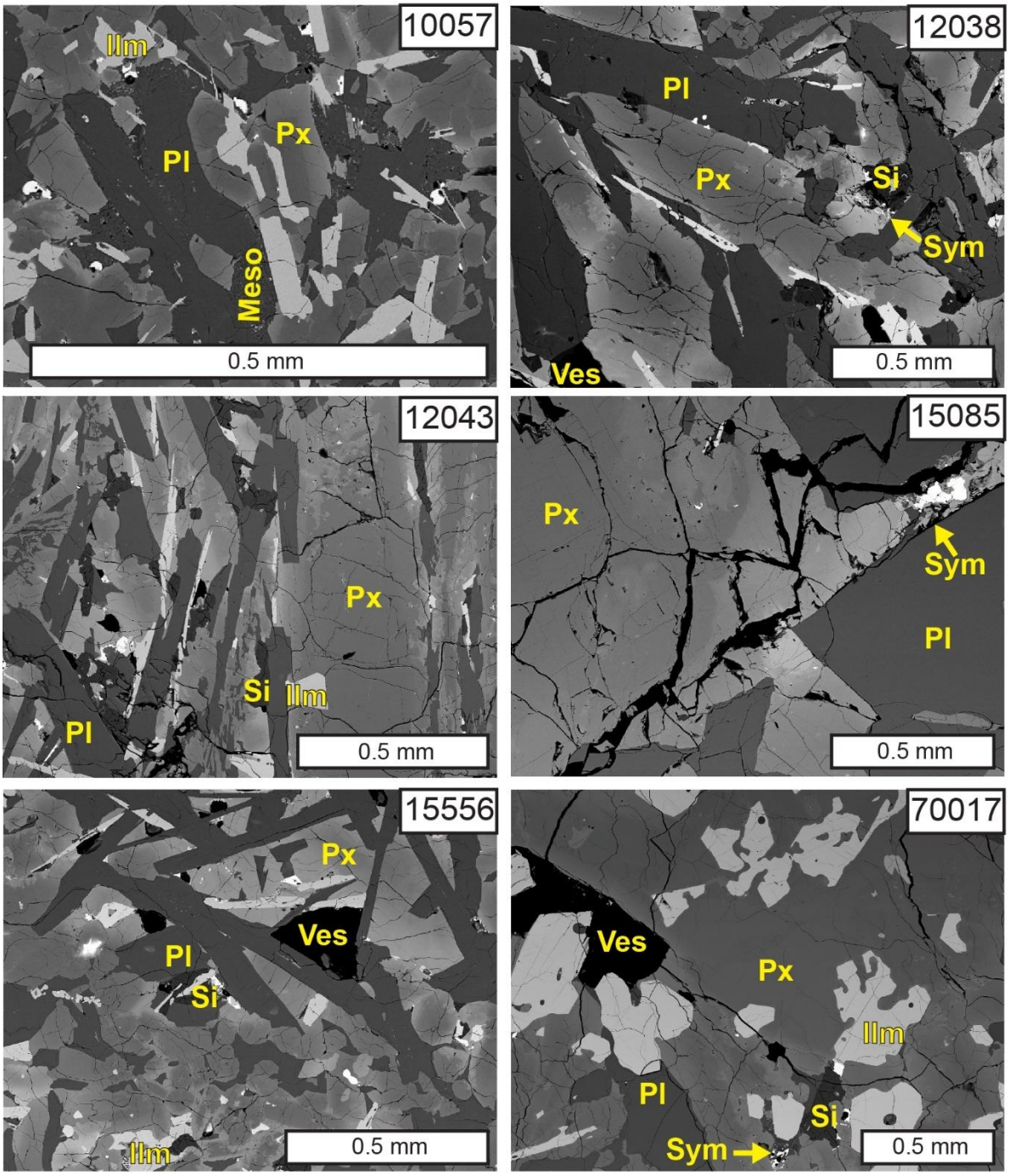

Fig. 3: Detail of sample textures imaged via SEM BSE. Annotations indicate the following components: Pl = plagioclase feldspar, Px = pyroxene, Ilm = ilmenite, Meso = mesostasis, Si = silica-rich phase, Sym = symplectites, Ves = vesicle.

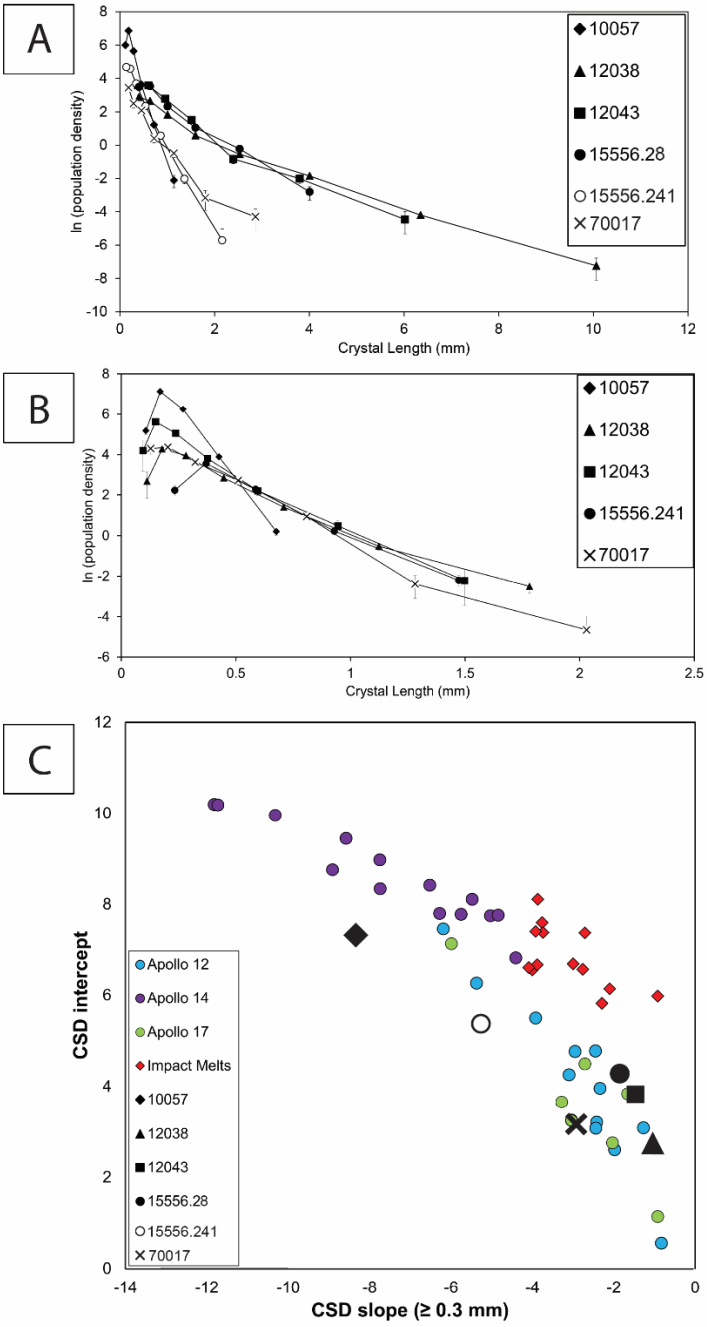

1239

1240 **Fig. 4: A**) CSDs of plagioclase feldspar in each sample; note that 15085 thin sections do not
1241 contain a representative number of plagioclase crystals for CSD analysis. **B**) ilmenite CSDs for
1242 each of the samples. Note that there were not enough crystals in thin section 15556,28, or in any
1243 thin sections of 15085, for representative ilmenite CSD analysis. **C**) The approximate CSD
1244 intercept and slope for plagioclase feldspar in each sample plotted against data collated in Neal et
1245 al. (2015).

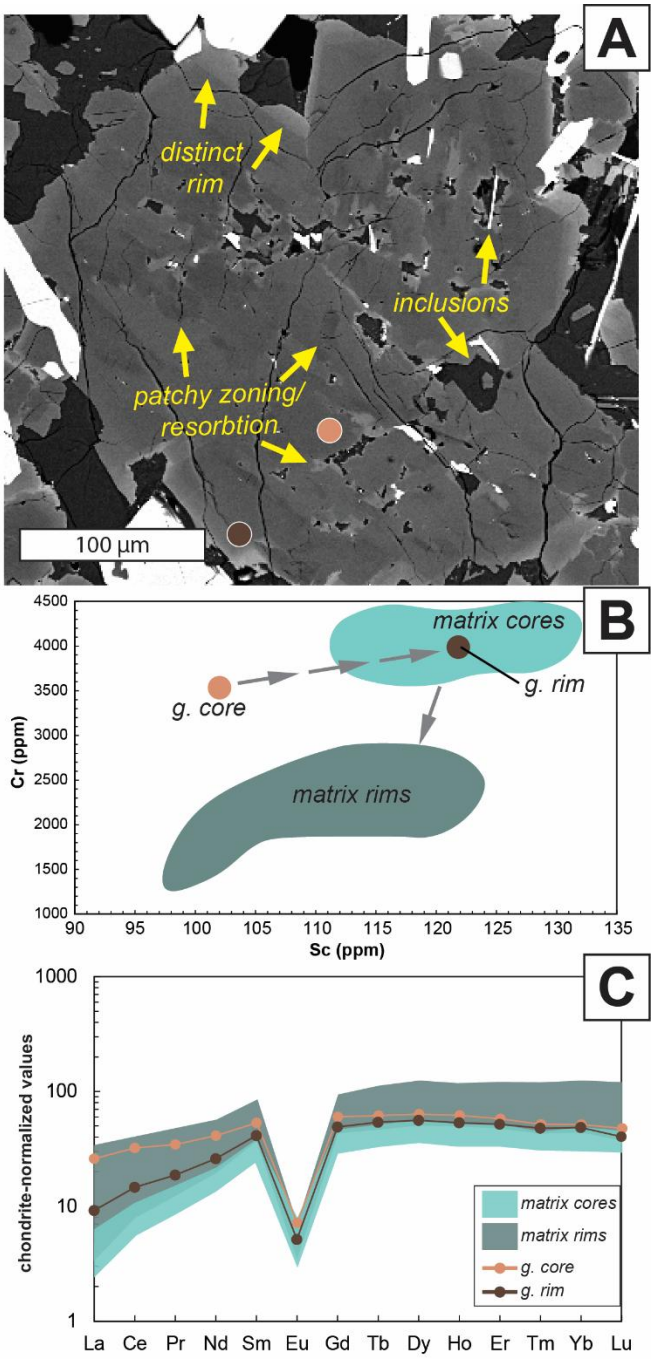

Fig. 5: Antecrystic glomerocryst identified in 10057. A) BSE image of the glomerocryst, with textural characteristics of interest highlighted with text/arrows. Color spots indicate locations of chemical analysis presented in panels B and C. B) Trace element content of the glomerocryst core and rim (g. core and g. rim, respectively) compared to surrounding matrix pyroxene. C) Rare earth element data of the glomerocryst core and rim (g. core and g. rim, respectively) compared to surrounding matrix pyroxene. For additional geochemical information see Figs. S4-S7 for plagioclase, and S8-S11 for pyroxene.

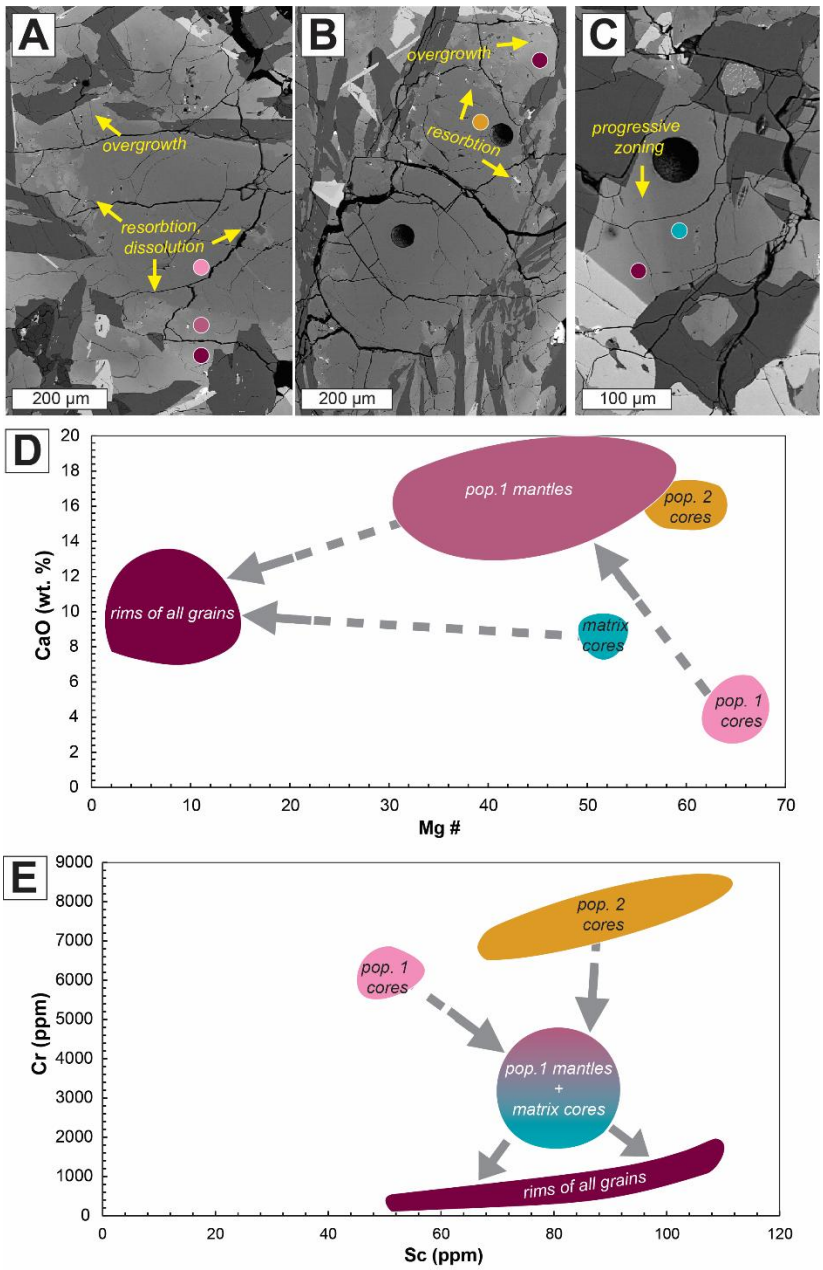

1254

1255 **Fig. 6**: The three unique pyroxene populations identified in 12043, including representative
1256 antecrystic pyroxene macrocrysts. A) represents the pigeonitic population 1, B) represents the
1257 augitic population 2, and C) represents the final matrix population 3. Textural features of interest
1258 are highlighted with yellow text and arrows. Color spots indicate representative locations of
1259 chemical analyses. D) Representative major element evolution of the identified pyroxene
1260 populations; colors of geochemical fields correspond to core/mantle/rim locations depicted in
1261 panels A-C. E) Representative trace element evolution of the identified pyroxene populations;
1262 colors of geochemical fields correspond to core/mantle/rim locations depicted in panels A-C. For
1263 additional geochemical information see Figs. S4-S7 for plagioclase, and S8-S11 for pyroxene.

1264

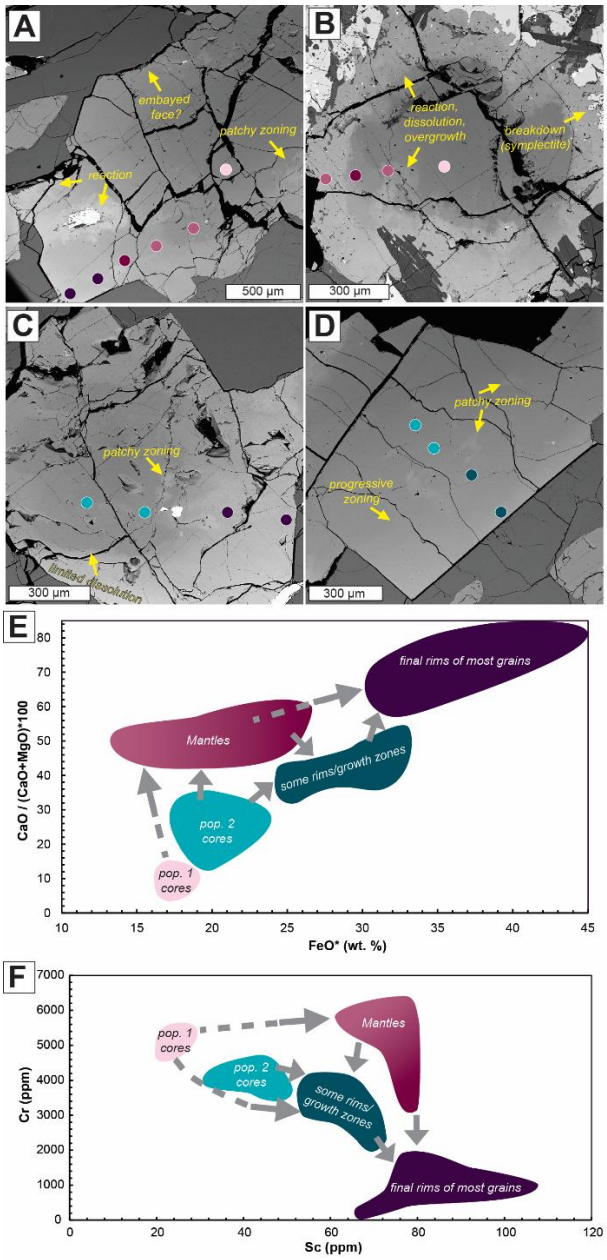

1265

1266 **Fig. 7**: Antecrystic pyroxene macrocrysts identified in 15085. A), B) Depict representative grains
1267 from the pyroxene population identified to be in greatest textural disequilibrium. Textural
1268 features of interest are highlighted with yellow text and arrows. Color spots indicate
1269 representative locations of chemical analyses. C) Pyroxene macrocryst representative of a second
1270 population with comparatively lower degree of textural disequilibrium. D) Matrix pyroxene with
1271 no textural disequilibrium, geochemically similar to population 2 (see panel C). E)
1272 Representative major element evolution of the identified pyroxene populations; colors of
1273 geochemical fields correspond to core/mantle/rim locations depicted in panels A-D. F)
1274 Representative trace element evolution of the identified pyroxene populations; colors of
1275 geochemical fields correspond to core/mantle/rim locations depicted in panels A-D. For
1276 additional geochemical information see Figs. S4-S7 for plagioclase, and S8-S11 for pyroxene.

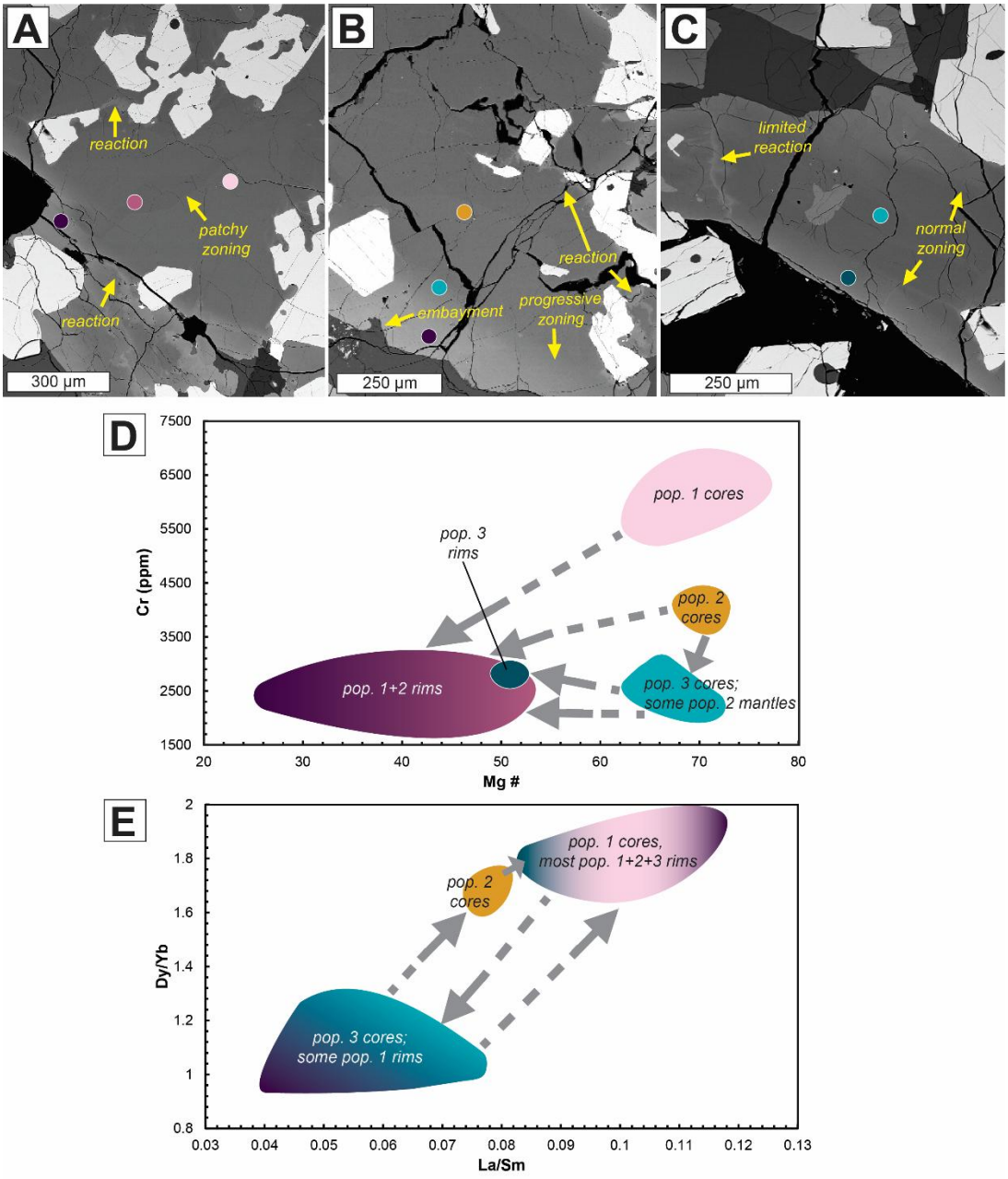

1277

1278 **Fig. 8**: Diverse magmatic features identified in 70017. Panels A-C depict the three unique
1279 pyroxene populations identified in this work; textural features of interest are highlighted with
1280 yellow text and arrows. Color spots indicate representative locations of chemical analyses. D)
1281 Representative geochemical evolution of the identified pyroxene populations; colors of
1282 geochemical fields correspond to core/mantle/rim locations depicted in panels A-C. E)
1283 Representative evolution of the identified pyroxene populations in the context of rare earth
1284 elements; colors of geochemical fields correspond to representative core/mantle/rim locations
1285 depicted in panels A-C. For additional geochemical information see Figs. S4-S7 for plagioclase,
1286 and S8-S11 for pyroxene.

1287

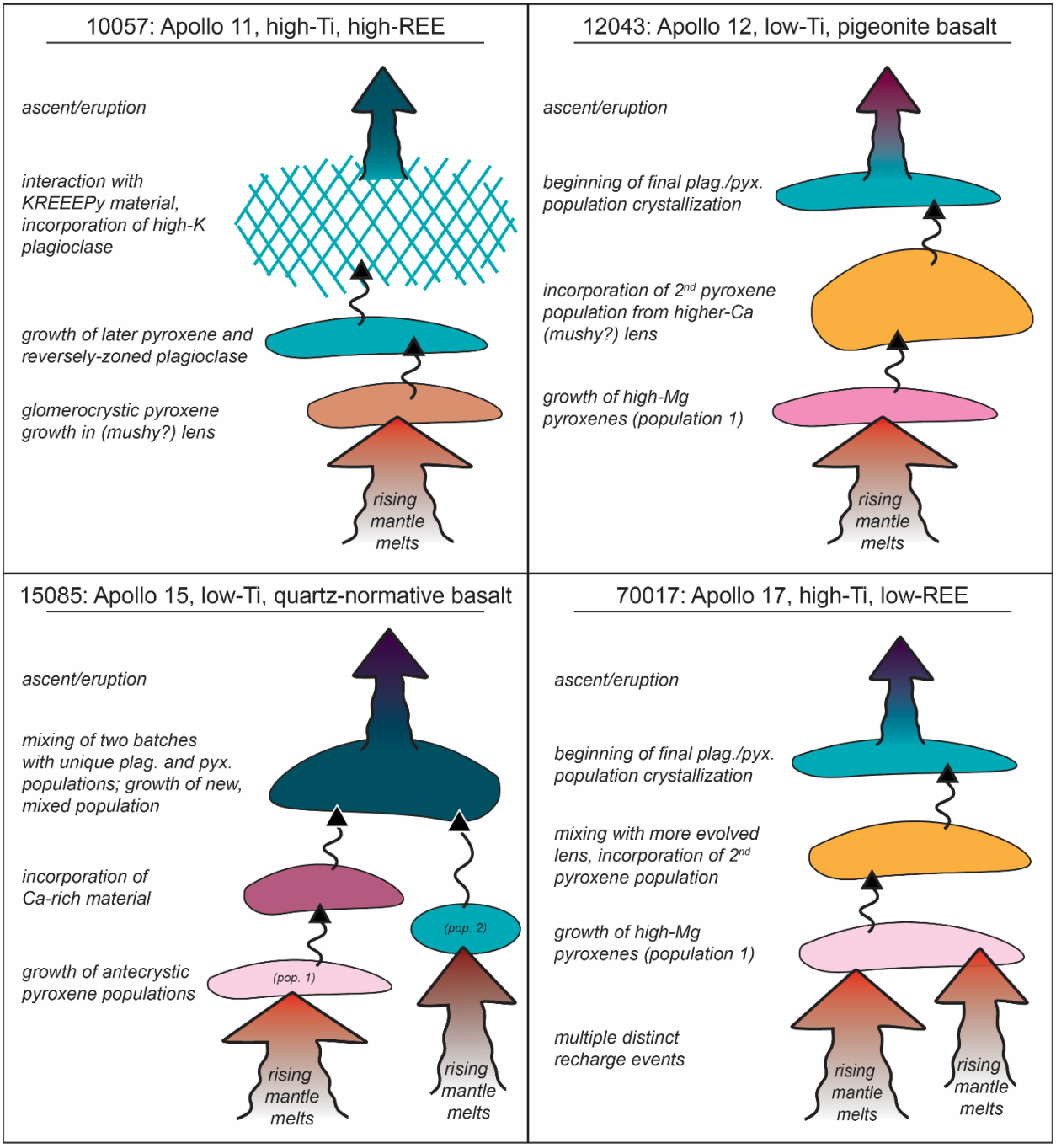

Fig. 9: Simplified cartoons of the possible plumbing system architectures for each of the four samples identified here to record open magmatic system processing. The cartoons are based on the diverse pyroxene and plagioclase crystal populations identified here in samples 10057, 12043, 15085, and 70017; see text for further explanation of sample crystallization sequences. Colors of system lenses correspond to the color-coded crystal growth stages identified in Figs. 5-8.

10. Supplemental Figures

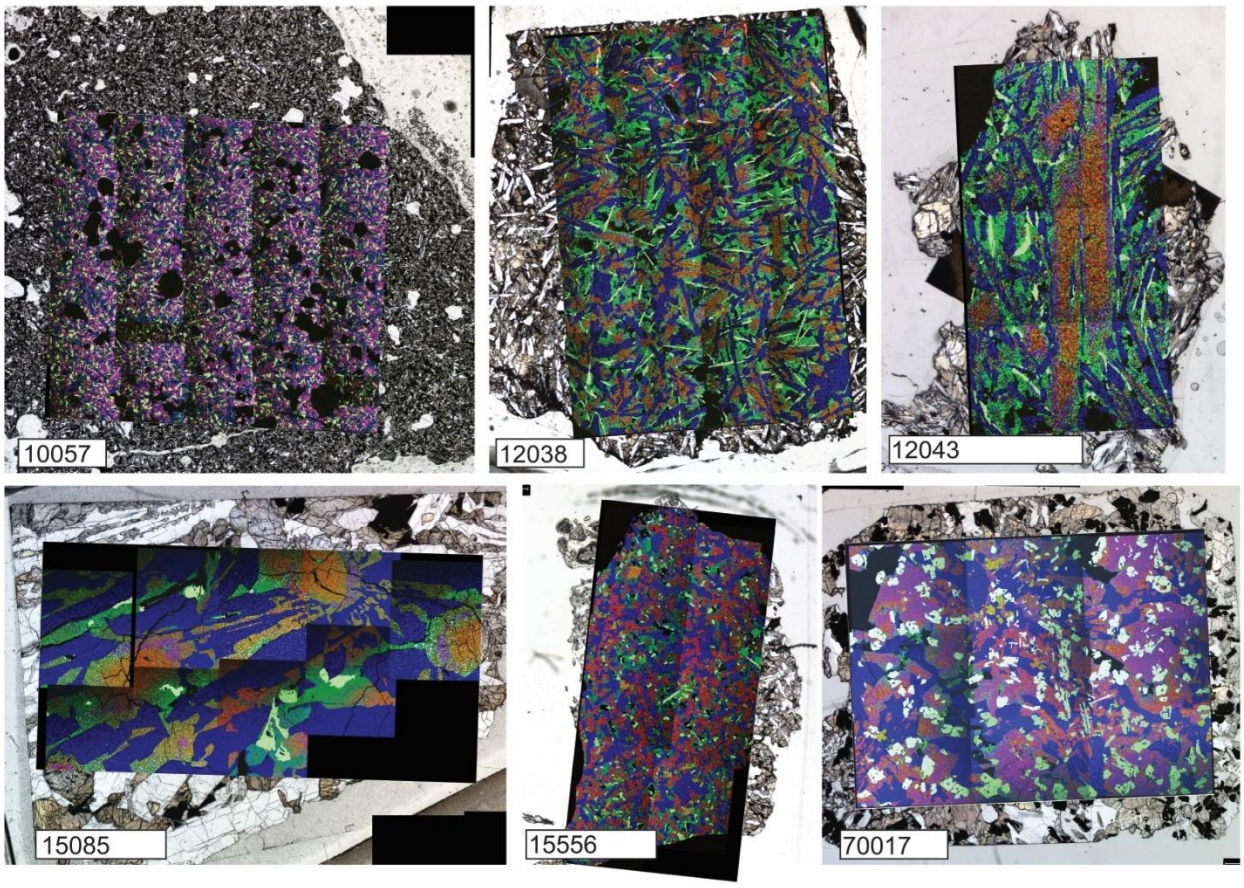

Fig. S1: SEM-EDS major elements maps: red is Mg, green is Fe, blue is Ca, white is Ti. Scalebars are 2.5 mm.

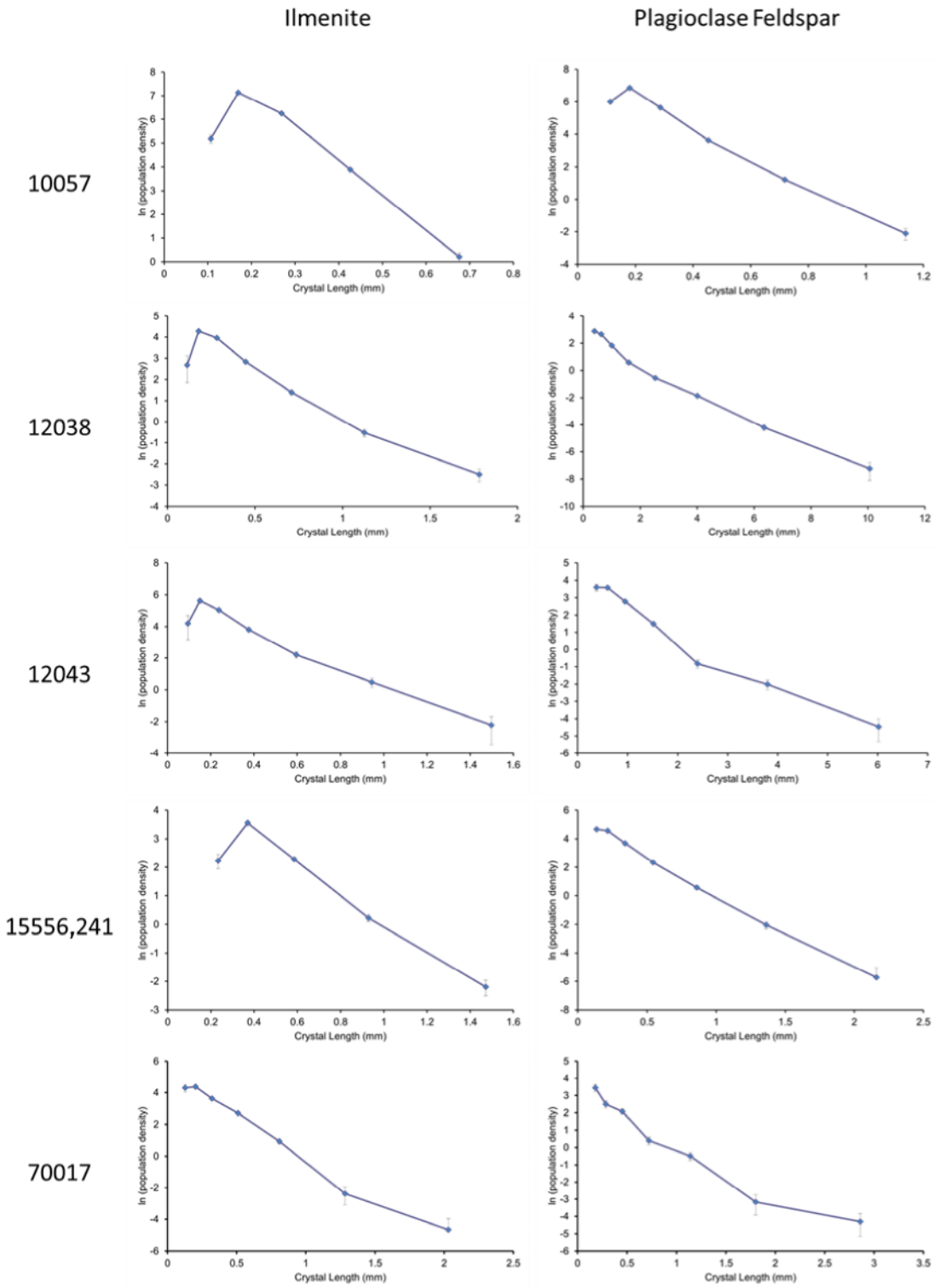

Fig. S2: Individual CSD plots for ilmenite and plagioclase feldspar in these samples; 15556.241 displayed as the more representative split based on crystal number (see Table S2). Error bars represent error calculated via *CSD Corrections* (Higgins, 2000).

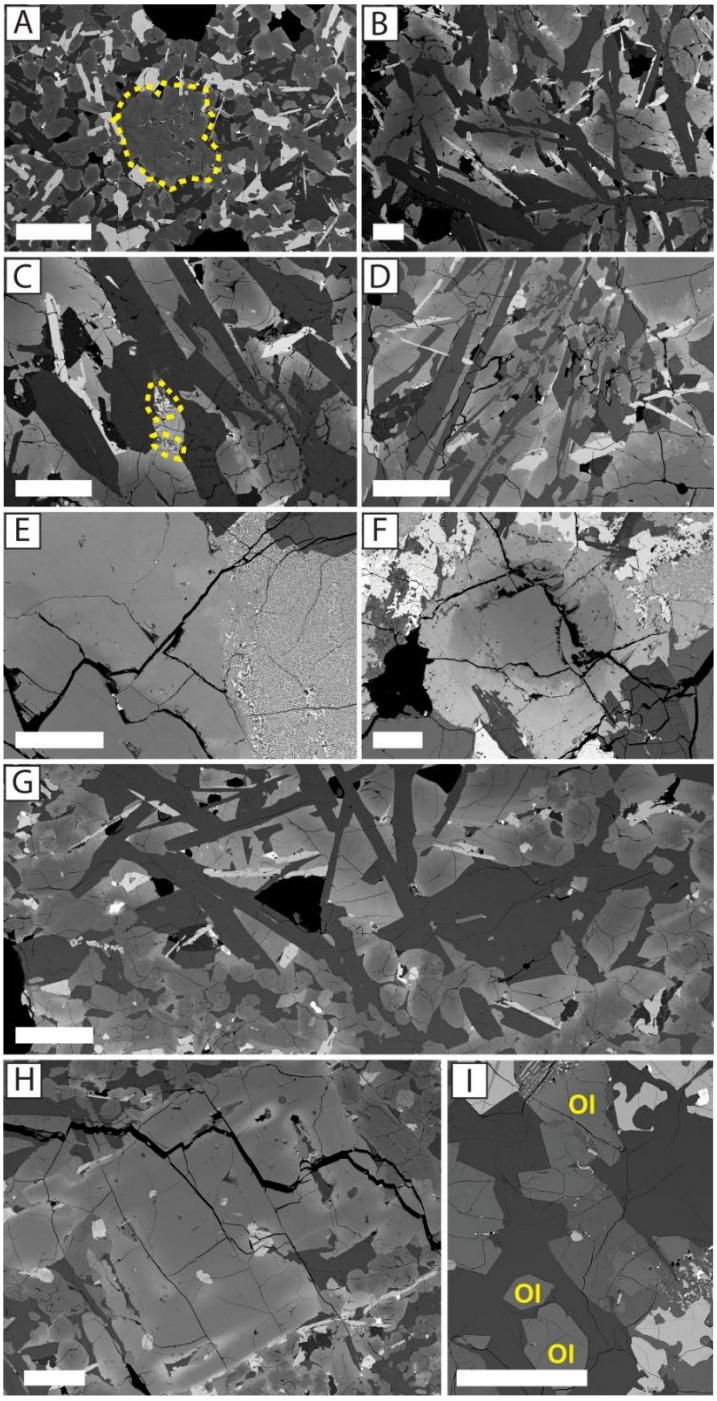

Fig. S3: Example grain textures in the studied samples; all scalebars are 250 μm. A) Glomerocryst in 10057 outlined by yellow dashed line. B) Plagioclase subophitically enclosed in pyroxene in 12038. C) Symplectite along pyroxene rims in 12038, outlined by yellow dashed lines. D) Pyroxene and feldspar matrix in 12043. E) Replacement of pyroxene by symplectite in 15085. F) Pyroxene with distinct zoning in 15085. G) Plagioclase feldspar clots in 15556 at top of the image – compared to interstitial texture of feldspar seen at the bottom of the image, typical of this sample. H) Macrocrystic olivine in 15556. I) Olivine grains in 70017.

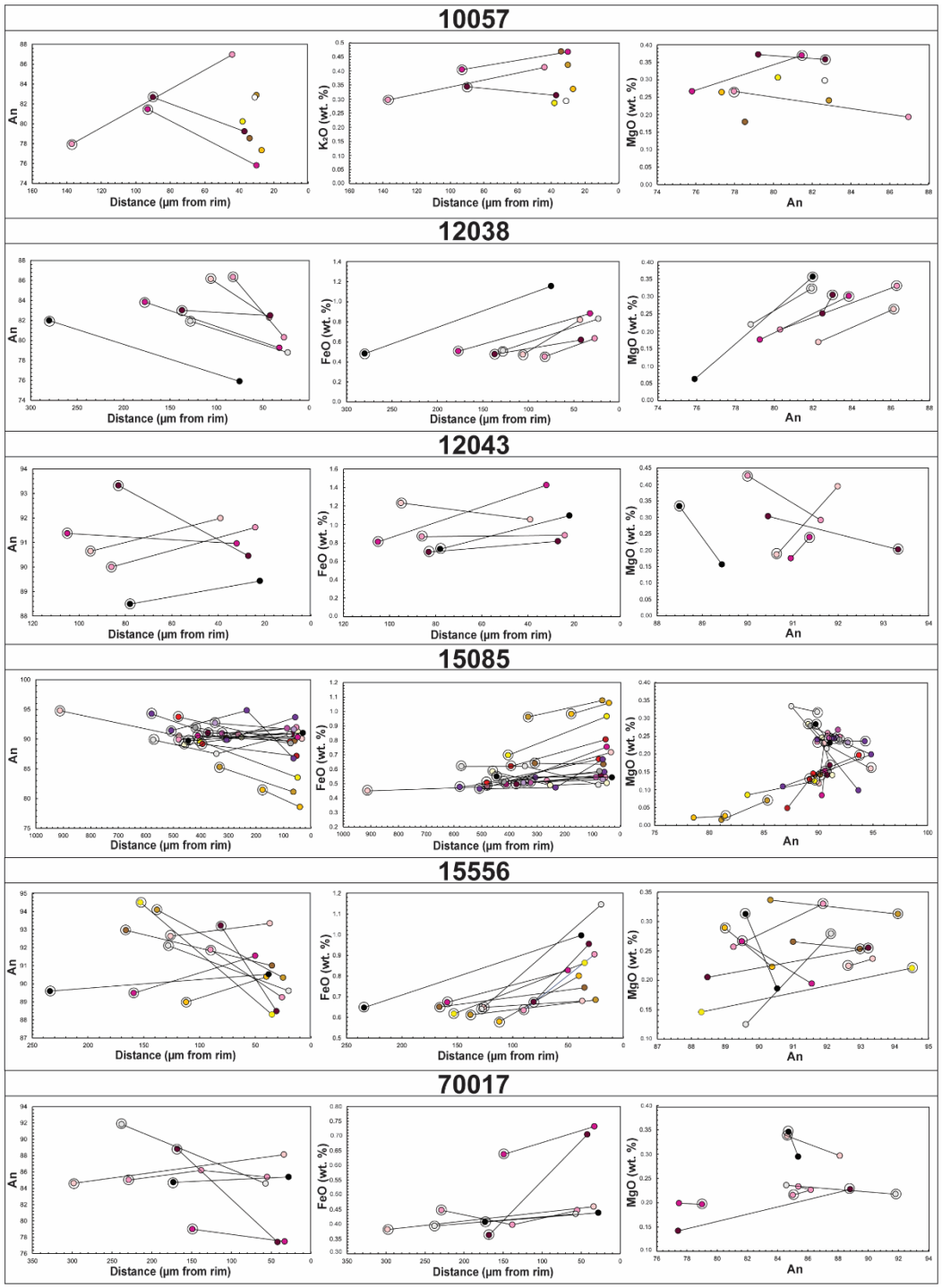

Fig. S4: Major element data for plagioclase feldspar grains studied here. Encircled points denote crystal cores; core-rim pairs are connected by a line. All distances in μm and represent distance from the grain rim.

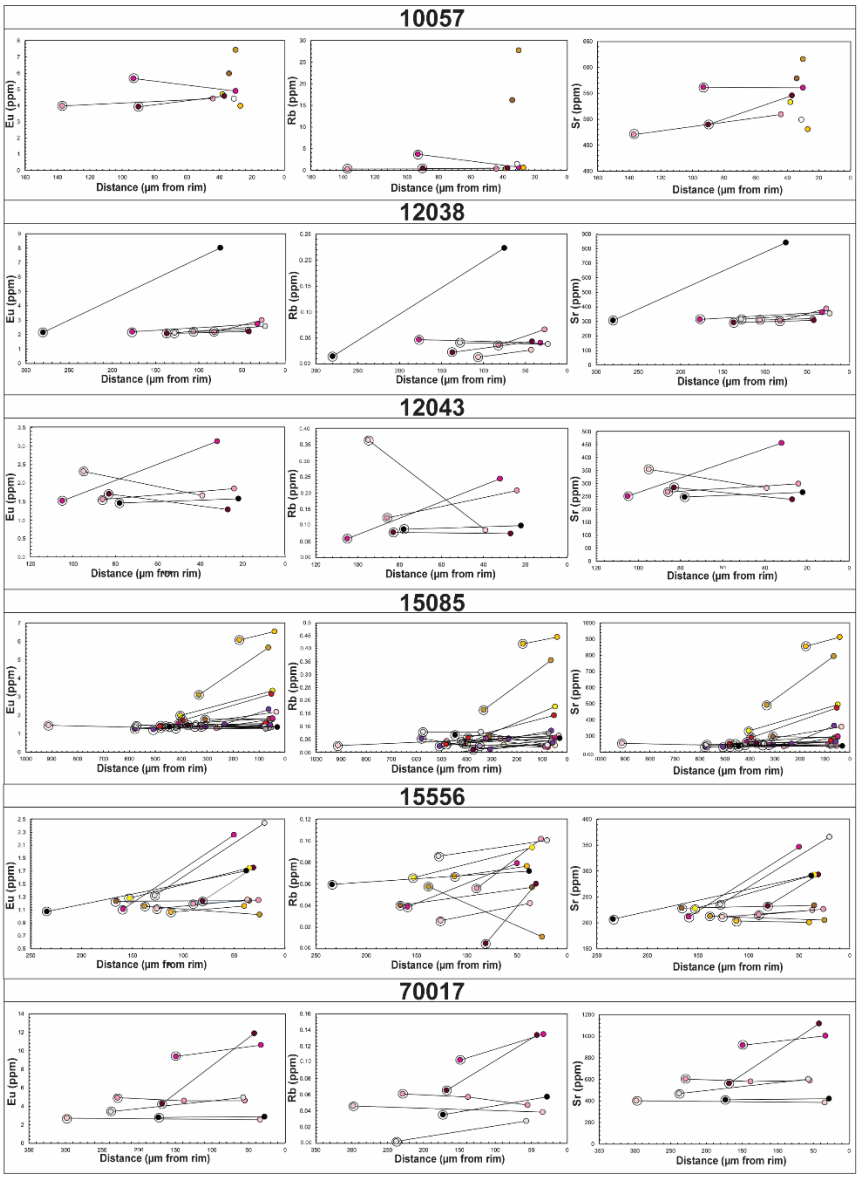

Fig. S5: Trace element data for plagioclase feldspar grains studied here. Encircled points denote crystal cores; core-rim pairs are connected by a line. All distances in μm and represent distance from the grain rim. Each grain is represented by a unique color; each color represents the same grain as those in Fig. S4.

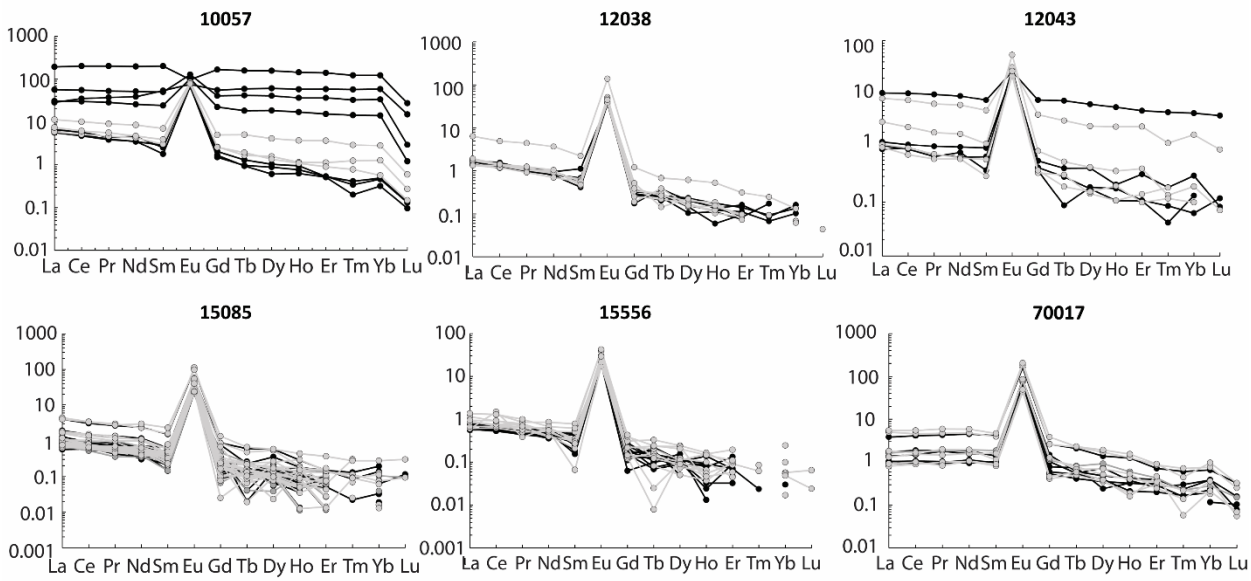

Fig. S6: Chondrite-normalized spidergrams of plagioclase feldspar analyses across the samples studied. Cores in black, rims in light gray.

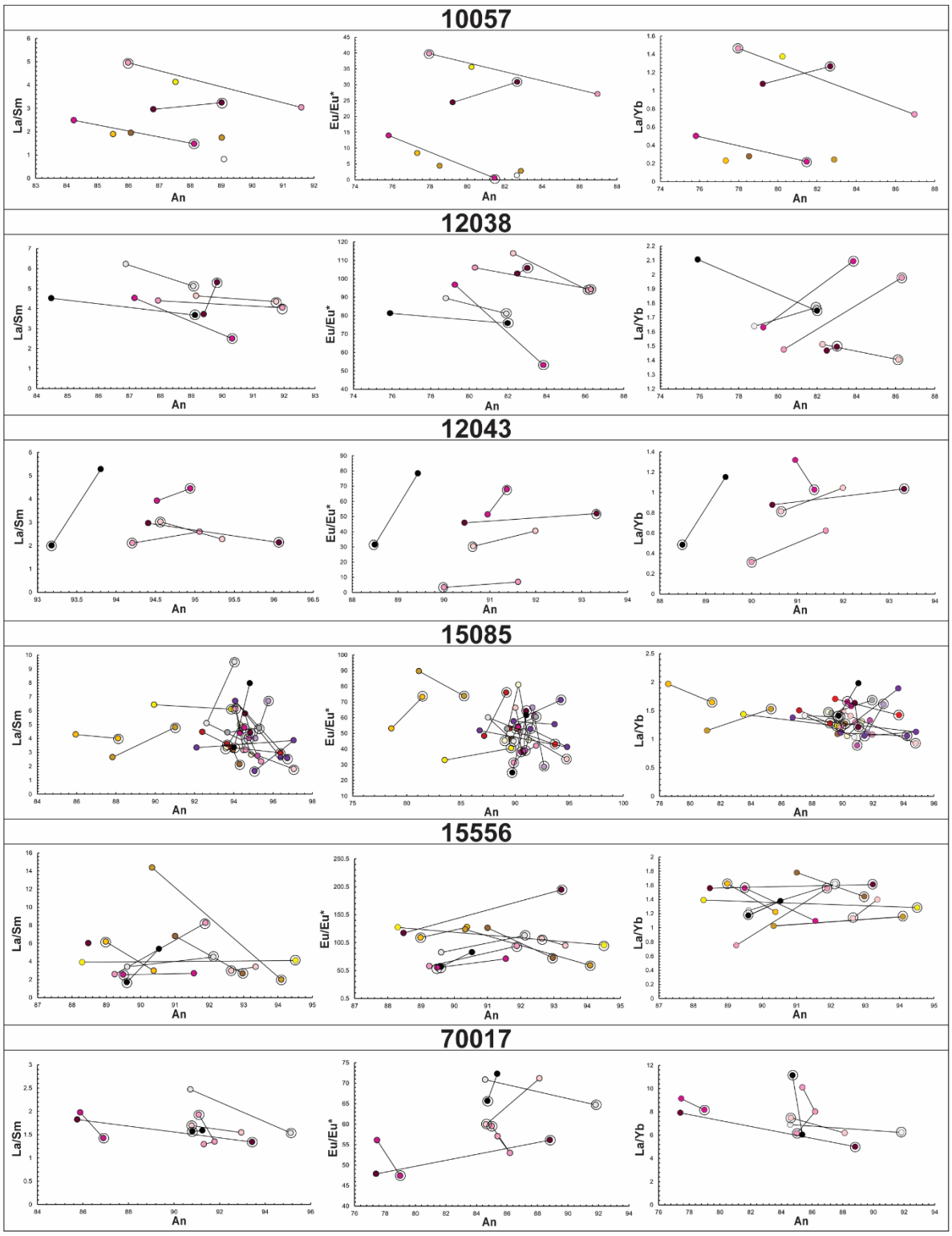

Fig. S7: Trace element ratios in plagioclase feldspar grains studied here. Graphs match color scheme of Figs. S4 and S5.

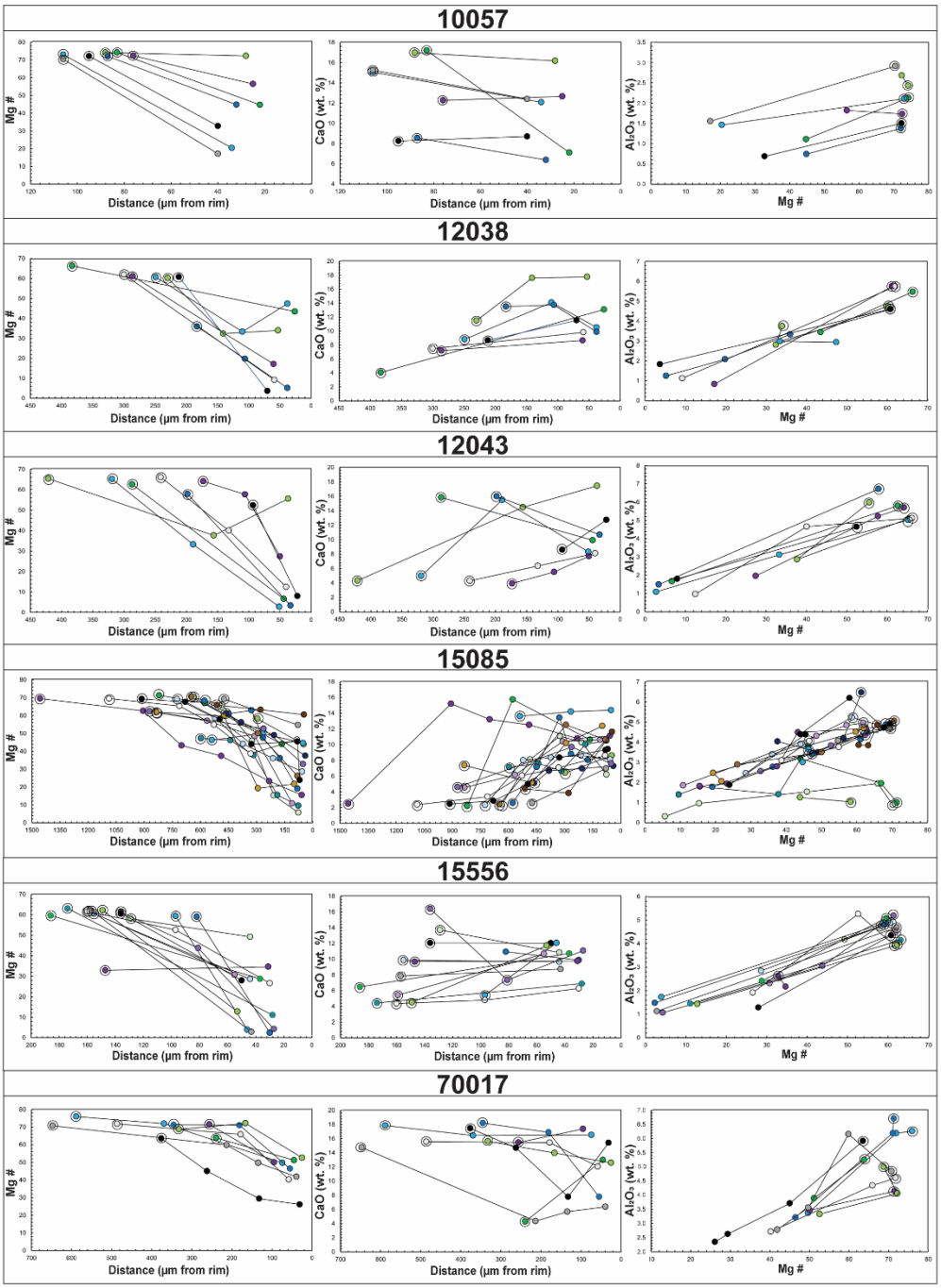

Fig. S8: Major element data for pyroxene grains studied here. Encircled points denote crystal cores; core-rim pairs are connected by a line. All distances in μm and represent distance from the grain rim.

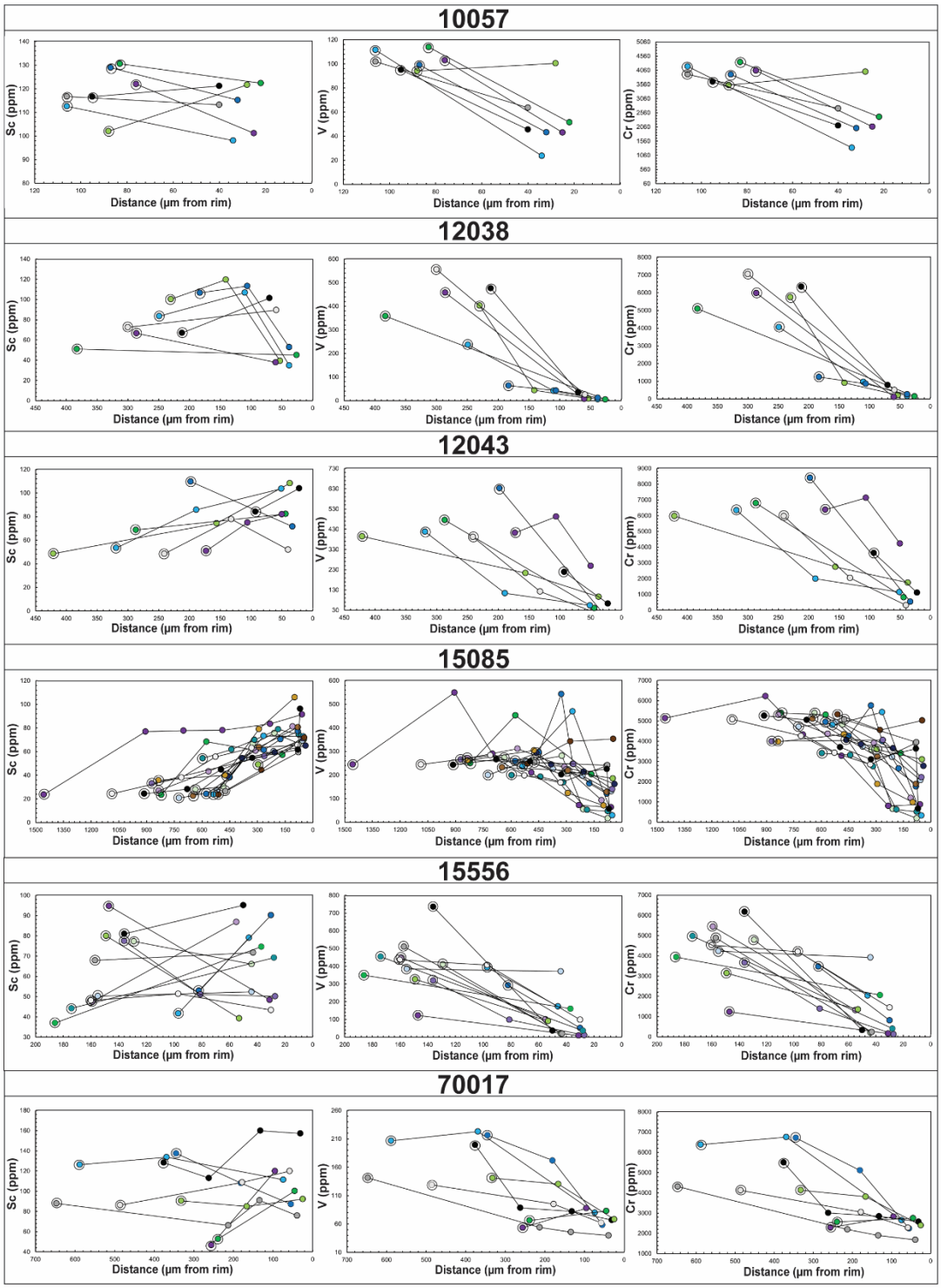

Fig. S9: Trace element data for pyroxene grains studied here. Encircled points denote crystal cores; core-rim pairs are connected by a line. All distances in μm and represent distance from the grain rim. Each grain is represented by a unique color; each color represents the same grain as those in Fig. S8.

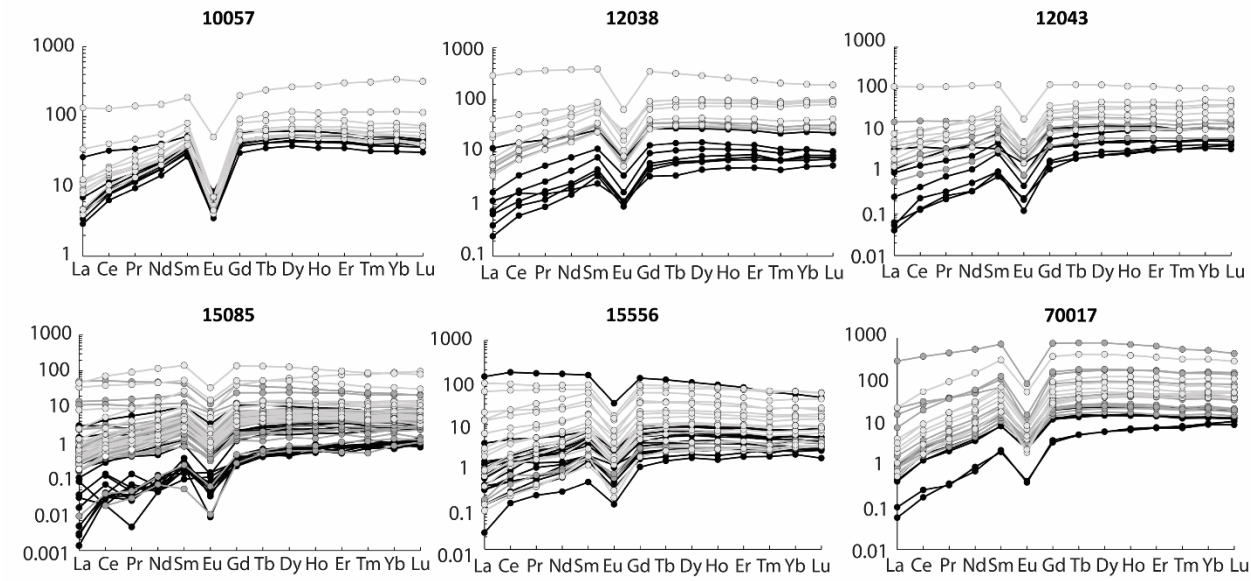

Fig. S10: Chondrite-normalized spidergrams of pyroxene analyses across the samples studied. Core analyses are in black, mantles in dark gray, and rims in light gray.

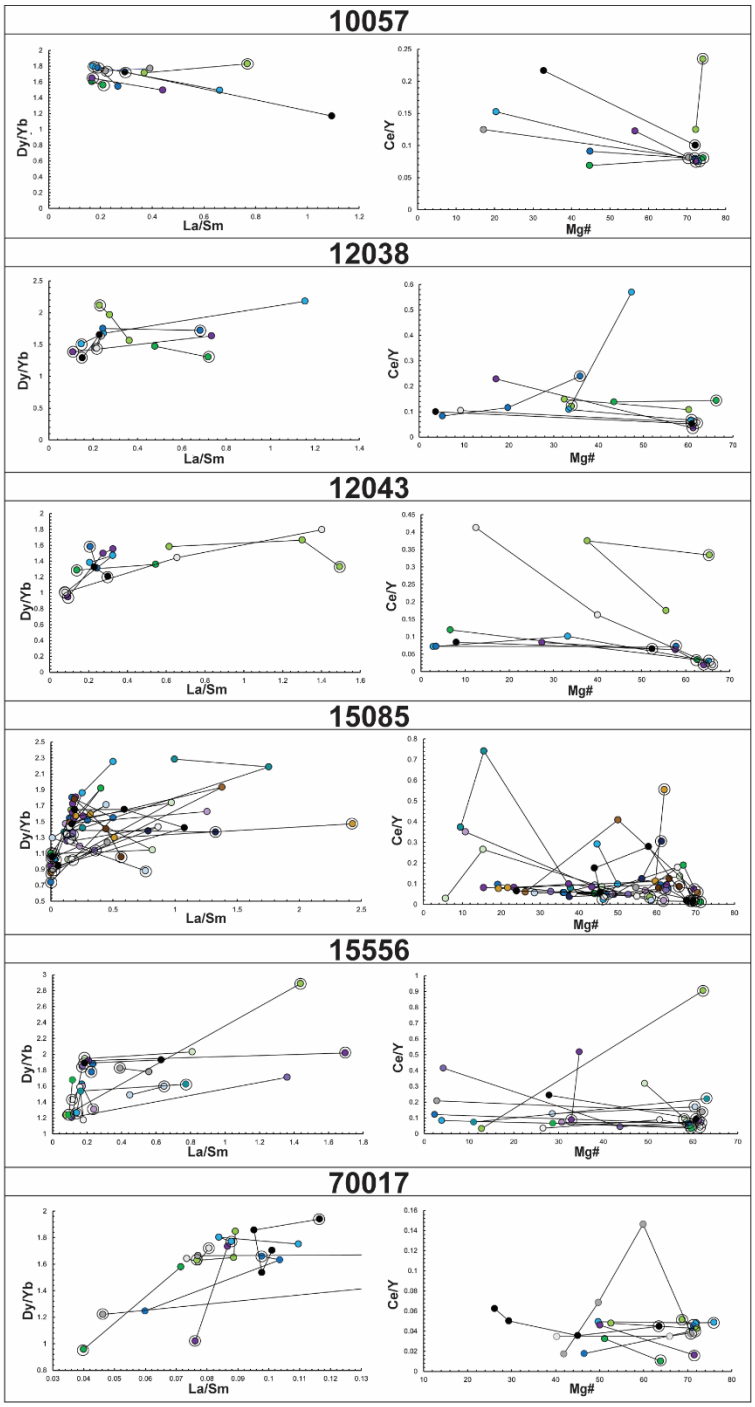

Fig. S11: Trace element ratios in pyroxene grains studied here. Graphs match color scheme of Figs. S8 and S9.

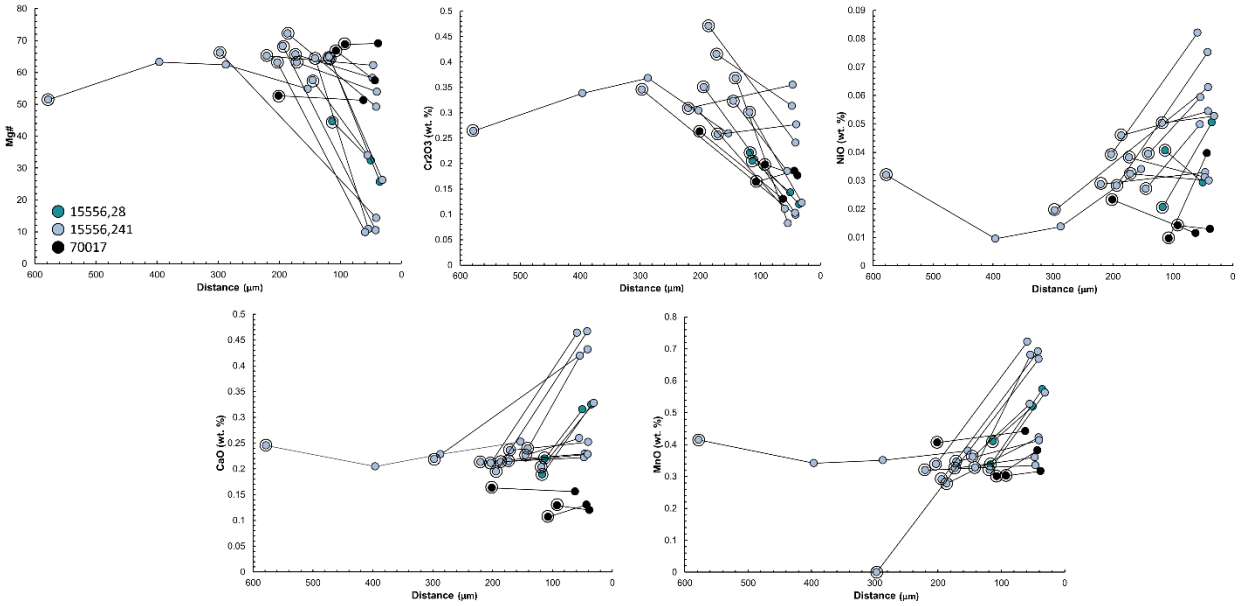

1350

1351 **Fig. S12:** Major and minor element data for olivine grains studied here. Encircled points mark
1352 the core of each grain; core rim pairs are connected by a line.